



CHORUS

This is the accepted manuscript made available via CHORUS. The article has been published as:

ϕ meson production in d+Au collisions at $\sqrt{s_{NN}}=200\text{GeV}$

A. Adare *et al.* (PHENIX Collaboration)

Phys. Rev. C **92**, 044909 — Published 19 October 2015

DOI: [10.1103/PhysRevC.92.044909](https://doi.org/10.1103/PhysRevC.92.044909)

ϕ meson production in d +Au collisions at $\sqrt{s_{NN}} = 200$ GeV

1

2 A. Adare,¹³ C. Aidala,^{42,43} N.N. Ajitanand,⁶² Y. Akiba,^{56,57} H. Al-Bataineh,⁵⁰ J. Alexander,⁶² M. Alfred,²³
3 A. Angerami,¹⁴ K. Aoki,^{31,34,56} N. Apadula,^{28,63} Y. Aramaki,^{12,56} H. Asano,^{34,56} E.T. Atomssa,³⁵ R. Averbeck,⁶³
4 T.C. Awes,⁵² B. Azmoun,⁷ V. Babintsev,²⁴ M. Bai,⁶ G. Baksay,¹⁹ L. Baksay,¹⁹ N.S. Bandara,⁴² B. Bannier,⁶³
5 K.N. Barish,⁸ B. Bassalleck,⁴⁹ A.T. Basye,¹ S. Bathe,^{5,8,57} V. Baublis,⁵⁵ C. Baumann,^{7,44} A. Bazilevsky,⁷
6 M. Beaumier,⁸ S. Beckman,¹³ S. Belikov,^{7,*} R. Belmont,^{43,67} R. Bennett,⁶³ A. Berdnikov,⁵⁹ Y. Berdnikov,⁵⁹
7 J.H. Bhom,⁷¹ D.S. Blau,³³ J.S. Bok,^{50,71} K. Boyle,^{57,63} M.L. Brooks,³⁸ J. Bryslawskyj,⁵ H. Buesching,⁷
8 V. Bumazhnov,²⁴ G. Bunce,^{7,57} S. Butsyk,³⁸ S. Campbell,^{14,28,63} A. Caringi,⁴⁵ C.-H. Chen,^{57,63} C.Y. Chi,¹⁴
9 M. Chiu,⁷ I.J. Choi,^{25,71} J.B. Choi,¹⁰ R.K. Choudhury,⁴ P. Christiansen,⁴⁰ T. Chujo,⁶⁶ P. Chung,⁶² O. Chvala,⁸
10 V. Cianciolo,⁵² Z. Citron,^{63,69} B.A. Cole,¹⁴ Z. Conesa del Valle,³⁵ M. Connors,⁶³ M. Csanád,¹⁷ T. Csörgő,⁷⁰
11 T. Dahms,⁶³ S. Dairaku,^{34,56} I. Danchev,⁶⁷ D. Danley,⁵¹ K. Das,²⁰ A. Datta,^{42,49} M.S. Daugherty,¹ G. David,⁷
12 M.K. Dayananda,²¹ K. DeBlasio,⁴⁹ K. Dehmelt,⁶³ A. Denisov,²⁴ A. Deshpande,^{57,63} E.J. Desmond,⁷
13 K.V. Dharmawardane,⁵⁰ O. Dietzsch,⁶⁰ A. Dion,^{28,63} P.B. Diss,⁴¹ J.H. Do,⁷¹ M. Donadelli,⁶⁰ L. D’Orazio,⁴¹
14 O. Drapier,³⁵ A. Drees,⁶³ K.A. Drees,⁶ J.M. Durham,^{38,63} A. Durum,²⁴ D. Dutta,⁴ S. Edwards,²⁰ Y.V. Efremenko,⁵²
15 F. Ellinghaus,¹³ T. Engelmores,¹⁴ A. Enokizono,^{52,56,58} H. En’yo,^{56,57} S. Esumi,⁶⁶ B. Fadem,⁴⁵ N. Feege,⁶³
16 D.E. Fields,⁴⁹ M. Finger,⁹ M. Finger, Jr.,⁹ F. Fleuret,³⁵ S.L. Fokin,³³ Z. Fraenkel,^{69,*} J.E. Frantz,^{51,63} A. Franz,⁷
17 A.D. Frawley,²⁰ K. Fujiwara,⁵⁶ Y. Fukao,⁵⁶ T. Fusayasu,⁴⁷ C. Gal,⁶³ P. Gallus,¹⁵ P. Garg,³ I. Garishvili,^{37,64}
18 H. Ge,⁶³ F. Giordano,²⁵ A. Glenn,³⁷ H. Gong,⁶³ M. Gonin,³⁵ Y. Goto,^{56,57} R. Granier de Cassagnac,³⁵ N. Grau,^{2,14}
19 S.V. Greene,⁶⁷ G. Grim,³⁸ M. Grosse Perdekamp,²⁵ T. Gunji,¹² H.-Å. Gustafsson,^{40,*} T. Hachiya,⁵⁶ J.S. Haggerty,⁷
20 K.I. Hahn,¹⁸ H. Hamagaki,¹² J. Hamblen,⁶⁴ H.F. Hamilton,¹ R. Han,⁵⁴ S.Y. Han,¹⁸ J. Hanks,^{14,63}
21 S. Hasegawa,²⁹ T.O.S. Haseler,²¹ K. Hashimoto,^{56,58} E. Haslum,⁴⁰ R. Hayano,¹² X. He,²¹ M. Heffner,³⁷
22 T.K. Hemmick,⁶³ T. Hester,⁸ J.C. Hill,²⁸ M. Hohlmann,¹⁹ R.S. Hollis,⁸ W. Holzmann,¹⁴ K. Homma,²² B. Hong,³²
23 T. Horaguchi,²² D. Hornback,⁶⁴ T. Hoshino,²² N. Hotvedt,²⁸ J. Huang,⁷ S. Huang,⁶⁷ T. Ichihara,^{56,57}
24 R. Ichimiya,⁵⁶ Y. Ikeda,⁶⁶ K. Imai,^{29,34,56} M. Inaba,⁶⁶ A. Iordanova,⁸ D. Isenhowe,¹ M. Ishihara,⁵⁶ M. Issah,⁶⁷
25 D. Ivanishchev,⁵⁵ Y. Iwanaga,²² B.V. Jacak,⁶³ M. Jezghani,²¹ J. Jia,^{7,62} X. Jiang,³⁸ J. Jin,¹⁴ B.M. Johnson,⁷
26 T. Jones,¹ K.S. Joo,⁴⁶ D. Jouan,⁵³ D.S. Jumper,^{1,25} F. Kajihara,¹² J. Kamin,⁶³ S. Kanda,¹² J.H. Kang,⁷¹
27 J. Kapustinsky,³⁸ K. Karatsu,^{34,56} M. Kasai,^{56,58} D. Kallow,^{42,57} M. Kawashima,^{56,58} A.V. Kazantsev,³³
28 T. Kempel,²⁸ J.A. Key,⁴⁹ V. Khachatryan,⁶³ A. Khazadzev,⁵⁵ K.M. Kijima,²² J. Kikuchi,⁶⁸ A. Kim,¹⁸ B.I. Kim,³²
29 C. Kim,³² D.J. Kim,³⁰ E.-J. Kim,¹⁰ G.W. Kim,¹⁸ M. Kim,⁶¹ Y.-J. Kim,²⁵ B. Kimelman,⁴⁵ E. Kinney,¹³ Á. Kiss,¹⁷
30 E. Kistenev,⁷ R. Kitamura,¹² J. Klatsky,²⁰ D. Kleinjan,⁸ P. Kline,⁶³ T. Koblesky,¹³ L. Kochenda,⁵⁵ B. Komkov,⁵⁵
31 M. Konno,⁶⁶ J. Koster,²⁵ D. Kotov,^{55,59} A. Král,¹⁵ A. Kravitz,¹⁴ G.J. Kunde,³⁸ K. Kurita,^{56,58} M. Kurosawa,^{56,57}
32 Y. Kwon,⁷¹ G.S. Kyle,⁵⁰ R. Lacey,⁶² Y.S. Lai,¹⁴ J.G. Lajoie,²⁸ A. Lebedev,²⁸ D.M. Lee,³⁸ J. Lee,¹⁸ K.B. Lee,³²
33 K.S. Lee,³² S. Lee,⁷¹ S.H. Lee,⁶³ M.J. Leitch,³⁸ M.A.L. Leite,⁶⁰ X. Li,¹¹ P. Lichtenwalner,⁴⁵ P. Liebing,⁵⁷
34 S.H. Lim,⁷¹ L.A. Linden Levy,¹³ T. Liška,¹⁵ H. Liu,³⁸ M.X. Liu,³⁸ B. Love,⁶⁷ D. Lynch,⁷ C.F. Maguire,⁶⁷
35 Y.I. Makdisi,⁶ M. Makek,⁷² M.D. Malik,⁴⁹ A. Manion,⁶³ V.I. Manko,³³ E. Mannel,^{7,14} Y. Mao,^{54,56} H. Masui,⁶⁶
36 F. Matathias,¹⁴ M. McCumber,^{38,63} P.L. McGaughey,³⁸ D. McGlinchey,^{13,20} C. McKinney,²⁵ N. Means,⁶³
37 A. Meles,⁵⁰ M. Mendoza,⁸ B. Meredith,²⁵ Y. Miake,⁶⁶ T. Mibe,³¹ A.C. Mignerey,⁴¹ K. Miki,^{56,66} A. Milov,^{7,69}
38 D.K. Mishra,⁴ J.T. Mitchell,⁷ S. Miyasaka,^{56,65} S. Mizuno,^{56,66} A.K. Mohanty,⁴ P. Montuenga,²⁵ H.J. Moon,⁴⁶
39 T. Moon,⁷¹ Y. Morino,¹² A. Morreale,⁸ D.P. Morrison,^{7,†} T.V. Moukhanova,³³ T. Murakami,^{34,56} J. Murata,^{56,58}
40 A. Mwai,⁶² S. Nagamiya,^{31,56} K. Nagashima,²² J.L. Nagle,^{13,‡} M. Naglis,⁶⁹ M.I. Nagy,^{17,70} I. Nakagawa,^{56,57}
41 H. Nakagomi,^{56,66} Y. Nakamiya,²² K.R. Nakamura,^{34,56} T. Nakamura,⁵⁶ K. Nakano,^{56,65} S. Nam,¹⁸ C. Nattrass,⁶⁴
42 P.K. Netrakanti,⁴ J. Newby,³⁷ M. Nguyen,⁶³ M. Nihashi,²² T. Niida,⁶⁶ S. Nishimura,¹² R. Nouicer,^{7,57} T. Novak,⁷⁰
43 N. Novitzky,^{30,63} A.S. Nyanin,³³ C. Oakley,²¹ E. O’Brien,⁷ S.X. Oda,¹² C.A. Ogilvie,²⁸ M. Oka,⁶⁶ K. Okada,⁵⁷
44 Y. Onuki,⁵⁶ J.D. Orjuela Koop,¹³ J.D. Osborn,⁴³ A. Oskarsson,⁴⁰ M. Ouchida,^{22,56} K. Ozawa,^{12,31} R. Pak,⁷
45 V. Pantuev,^{26,63} V. Papavassiliou,⁵⁰ I.H. Park,¹⁸ J.S. Park,⁶¹ S. Park,⁶¹ S.K. Park,³² W.J. Park,³² S.F. Pate,⁵⁰
46 M. Patel,²⁸ H. Pei,²⁸ J.-C. Peng,²⁵ H. Pereira,¹⁶ D.V. Perepelitsa,⁷ G.D.N. Perera,⁵⁰ D.Yu. Peressounko,³³
47 J. Perry,²⁸ R. Petti,^{7,63} C. Pinkenburg,⁷ R. Pinson,¹ R.P. Pisani,⁷ M. Proissl,⁶³ M.L. Purschke,⁷ H. Qu,²¹
48 J. Rak,³⁰ B.J. Ramson,⁴³ I. Ravinovich,⁶⁹ K.F. Read,^{52,64} S. Rembeczki,¹⁹ K. Reygers,⁴⁴ D. Reynolds,⁶²
49 V. Riabov,^{48,55} Y. Riabov,^{55,59} E. Richardson,⁴¹ T. Rinn,²⁸ D. Roach,⁶⁷ G. Roche,^{39,*} S.D. Rolnick,⁸ M. Rosati,²⁸
50 C.A. Rosen,¹³ S.S.E. Rosendahl,⁴⁰ Z. Rowan,⁵ J.G. Rubin,⁴³ P. Ružička,²⁷ B. Sahlmueller,^{44,63} N. Saito,³¹
51 T. Sakaguchi,⁷ K. Sakashita,^{56,65} H. Sako,²⁹ V. Samsonov,^{48,55} S. Sano,^{12,68} M. Sarsour,²¹ S. Sato,^{29,31} T. Sato,⁶⁶
52 S. Sawada,³¹ B. Schaefer,⁶⁷ B.K. Schmoll,⁶⁴ K. Sedgwick,⁸ J. Seele,¹³ R. Seidl,^{25,56,57} A. Sen,⁶⁴ R. Seto,⁸

53 P. Sett,⁴ A. Sexton,⁴¹ D. Sharma,^{63,69} I. Shein,²⁴ T.-A. Shibata,^{56,65} K. Shigaki,²² M. Shimomura,^{28,66}
 54 K. Shoji,^{34,56} P. Shukla,⁴ A. Sickles,^{7,25} C.L. Silva,^{28,38} D. Silvermyr,^{40,52} C. Silvestre,¹⁶ K.S. Sim,³² B.K. Singh,³
 55 C.P. Singh,³ V. Singh,³ M. Slunečka,⁹ M. Snowball,³⁸ R.A. Soltz,³⁷ W.E. Sondheim,³⁸ S.P. Sorensen,⁶⁴
 56 I.V. Sourikova,⁷ P.W. Stankus,⁵² E. Stenlund,⁴⁰ M. Stepanov,^{42,50,*} S.P. Stoll,⁷ T. Sugitate,²² A. Sukhanov,⁷
 57 T. Sumita,⁵⁶ J. Sun,⁶³ J. Sziklai,⁷⁰ E.M. Takagui,⁶⁰ A. Taketani,^{56,57} R. Tanabe,⁶⁶ Y. Tanaka,⁴⁷ S. Taneja,⁶³
 58 K. Tanida,^{34,56,57,61} M.J. Tannenbaum,⁷ S. Tarafdar,^{3,69} A. Taranenko,^{48,62} H. Themann,⁶³ D. Thomas,¹
 59 T.L. Thomas,⁴⁹ R. Tieulent,²¹ A. Timilsina,²⁸ T. Todoroki,^{56,66} M. Togawa,⁵⁷ A. Toia,⁶³ L. Tomášek,²⁷
 60 M. Tomášek,^{15,27} H. Torii,²² C.L. Towell,¹ R. Towell,¹ R.S. Towell,¹ I. Tserruya,⁶⁹ Y. Tsuchimoto,²² C. Vale,⁷
 61 H. Valle,⁶⁷ H.W. van Hecke,³⁸ E. Vazquez-Zambrano,¹⁴ A. Veicht,^{14,25} J. Velkovska,⁶⁷ R. Vértesi,⁷⁰ M. Virius,¹⁵
 62 V. Vrba,^{15,27} E. Vznuzdaev,⁵⁵ X.R. Wang,^{50,57} D. Watanabe,²² K. Watanabe,⁶⁶ Y. Watanabe,^{56,57}
 63 Y.S. Watanabe,^{12,31} F. Wei,^{28,50} R. Wei,⁶² J. Wessels,⁴⁴ A.S. White,⁴³ S.N. White,⁷ D. Winter,¹⁴
 64 C.L. Woody,⁷ R.M. Wright,¹ M. Wysocki,^{13,52} B. Xia,⁵¹ L. Xue,²¹ S. Yalcin,⁶³ Y.L. Yamaguchi,^{12,56,63}
 65 K. Yamaura,²² R. Yang,²⁵ A. Yanovich,²⁴ J. Ying,²¹ S. Yokkaichi,^{56,57} J.H. Yoo,³² I. Yoon,⁶¹ Z. You,⁵⁴
 66 G.R. Young,⁵² I. Younus,^{36,49} H. Yu,⁵⁴ I.E. Yushmanov,³³ W.A. Zajc,¹⁴ A. Zelenski,⁶ S. Zhou,¹¹ and L. Zou⁸

(PHENIX Collaboration)

¹Abilene Christian University, Abilene, Texas 79699, USA

²Department of Physics, Augustana College, Sioux Falls, South Dakota 57197, USA

³Department of Physics, Banaras Hindu University, Varanasi 221005, India

⁴Bhabha Atomic Research Centre, Bombay 400 085, India

⁵Baruch College, City University of New York, New York, New York, 10010 USA

⁶Collider-Accelerator Department, Brookhaven National Laboratory, Upton, New York 11973%-5000, USA

⁷Physics Department, Brookhaven National Laboratory, Upton, New York 11973%-5000, USA

⁸University of California-Riverside, Riverside, California 92521, USA

⁹Charles University, Ovocný trh 5, Praha 1, 116 36, Prague, Czech Republic

¹⁰Chonbuk National University, Jeonju, 561%-756, Korea

¹¹Science and Technology on Nuclear Data Laboratory, China Institute of Atomic Energy, Beijing 102413, P. R. China

¹²Center for Nuclear Study, Graduate School of Science, University of Tokyo, 7%-3%-1 Hongo, Bunkyo, Tokyo 113%-0033, Japan

¹³University of Colorado, Boulder, Colorado 80309, USA

¹⁴Columbia University, New York, New York 10027 and Nevis Laboratories, Irvington, New York 10533, USA

¹⁵Czech Technical University, Zikova 4, 166 36 Prague 6, Czech Republic

¹⁶Dapnia, CEA Saclay, F-91191, Gif-sur-Yvette, France

¹⁷ELTE, Eötvös Loránd University, H-1117 Budapest, Pázmány P. s. 1/A, Hungary

¹⁸Ewha Womans University, Seoul 120-750, Korea

¹⁹Florida Institute of Technology, Melbourne, Florida 32901, USA

²⁰Florida State University, Tallahassee, Florida 32306, USA

²¹Georgia State University, Atlanta, Georgia 30303, USA

²²Hiroshima University, Kagamiyama, Higashi-Hiroshima 739%-8526, Japan

²³Department of Physics and Astronomy, Howard University, Washington, DC 20059, USA

²⁴IHEP Protvino, State Research Center of Russian Federation, Institute for High Energy Physics, Protvino, 142281, Russia

²⁵University of Illinois at Urbana-Champaign, Urbana, Illinois 61801, USA

²⁶Institute for Nuclear Research of the Russian Academy of Sciences, propekt 60%-letiya Oktyabrya 7a, Moscow 117312, Russia

²⁷Institute of Physics, Academy of Sciences of the Czech Republic, Na Slovance 2, 182 21 Prague 8, Czech Republic

²⁸Iowa State University, Ames, Iowa 50011, USA

²⁹Advanced Science Research Center, Japan Atomic Energy Agency, 2%-4 Shirakata Shirane, Tokai-mura, Naka-gun, Ibaraki-ken 319%-1195, Japan

³⁰Helsinki Institute of Physics and University of Jyväskylä, P.O.Box 35, FI-40014 Jyväskylä, Finland

³¹KEK, High Energy Accelerator Research Organization, Tsukuba, Ibaraki 305%-0801, Japan

³²Korea University, Seoul, 136%-701, Korea

³³Russian Research Center "Kurchatov Institute", Moscow, 123098 Russia

³⁴Kyoto University, Kyoto 606%-8502, Japan

³⁵Laboratoire Leprince-Ringuet, Ecole Polytechnique, CNRS-IN2P3, Route de Saclay, F-91128, Palaiseau, France

³⁶Physics Department, Lahore University of Management Sciences, Lahore 54792, Pakistan

³⁷Lawrence Livermore National Laboratory, Livermore, California 94550, USA

³⁸Los Alamos National Laboratory, Los Alamos, New Mexico 87545, USA

³⁹LPC, Université Blaise Pascal, CNRS-IN2P3, Clermont-Fd, 63177 Aubiere Cedex, France

⁴⁰Department of Physics, Lund University, Box 118, SE-221 00 Lund, Sweden

⁴¹University of Maryland, College Park, Maryland 20742, USA

⁴²Department of Physics, University of Massachusetts, Amherst, Massachusetts 01003%-9337, USA

⁴³Department of Physics, University of Michigan, Ann Arbor, Michigan 48109%-1040, USA

- 113 ⁴⁴*Institut für Kernphysik, University of Muenster, D-48149 Muenster, Germany*
 114 ⁴⁵*Muhlenberg College, Allentown, Pennsylvania 18104-5586, USA*
 115 ⁴⁶*Myongji University, Yongin, Kyonggido 449-728, Korea*
 116 ⁴⁷*Nagasaki Institute of Applied Science, Nagasaki-shi, Nagasaki 851-0193, Japan*
 117 ⁴⁸*National Research Nuclear University, MEPhI, Moscow Engineering Physics Institute, Moscow, 115409, Russia*
 118 ⁴⁹*University of New Mexico, Albuquerque, New Mexico 87131, USA*
 119 ⁵⁰*New Mexico State University, Las Cruces, New Mexico 88003, USA*
 120 ⁵¹*Department of Physics and Astronomy, Ohio University, Athens, Ohio 45701, USA*
 121 ⁵²*Oak Ridge National Laboratory, Oak Ridge, Tennessee 37831, USA*
 122 ⁵³*IPN-Orsay, Universite Paris Sud, CNRS-IN2P3, BP1, F-91406, Orsay, France*
 123 ⁵⁴*Peking University, Beijing 100871, P. R. China*
 124 ⁵⁵*PNPI, Petersburg Nuclear Physics Institute, Gatchina, Leningrad region, 188300, Russia*
 125 ⁵⁶*RIKEN Nishina Center for Accelerator-Based Science, Wako, Saitama 351-0198, Japan*
 126 ⁵⁷*RIKEN BNL Research Center, Brookhaven National Laboratory, Upton, New York 11973-5000, USA*
 127 ⁵⁸*Physics Department, Rikkyo University, 3-34-1 Nishi-Ikebukuro, Toshima, Tokyo 171-8501, Japan*
 128 ⁵⁹*Saint Petersburg State Polytechnic University, St. Petersburg, 195251 Russia*
 129 ⁶⁰*Universidade de São Paulo, Instituto de Física, Caixa Postal 66318, São Paulo CEP05315-970, Brazil*
 130 ⁶¹*Department of Physics and Astronomy, Seoul National University, Seoul 151-742, Korea*
 131 ⁶²*Chemistry Department, Stony Brook University, SUNY, Stony Brook, New York 11794-3400, USA*
 132 ⁶³*Department of Physics and Astronomy, Stony Brook University, SUNY, Stony Brook, New York 11794-3800, USA*
 133 ⁶⁴*University of Tennessee, Knoxville, Tennessee 37996, USA*
 134 ⁶⁵*Department of Physics, Tokyo Institute of Technology, Oh-okayama, Meguro, Tokyo 152-8551, Japan*
 135 ⁶⁶*Institute of Physics, University of Tsukuba, Tsukuba, Ibaraki 305, Japan*
 136 ⁶⁷*Vanderbilt University, Nashville, Tennessee 37235, USA*
 137 ⁶⁸*Waseda University, Advanced Research Institute for Science and*
 138 *Engineering, 17 Kikui-cho, Shinjuku-ku, Tokyo 162-0044, Japan*
 139 ⁶⁹*Weizmann Institute, Rehovot 76100, Israel*
 140 ⁷⁰*Institute for Particle and Nuclear Physics, Wigner Research Centre for Physics, Hungarian*
 141 *Academy of Sciences (Wigner RCP, RMKI) H-1525 Budapest 114, POBox 49, Budapest, Hungary*
 142 ⁷¹*Yonsei University, IPAP, Seoul 120-749, Korea*
 143 ⁷²*University of Zagreb, Faculty of Science, Department of Physics, Bijenička 32, HR-10002 Zagreb, Croatia*

The PHENIX collaboration has measured ϕ meson production in d +Au collisions at $\sqrt{s_{NN}} = 200$ GeV using the dimuon and dielectron decay channels. The ϕ meson is measured in the forward (backward) d -going (Au-going) direction, $1.2 < y < 2.2$ ($-2.2 < y < -1.2$) in the transverse-momentum (p_T) range from 1–7 GeV/ c , and at midrapidity $|y| < 0.35$ in the p_T range below 7 GeV/ c . The ϕ meson invariant yields and nuclear-modification factors as a function of p_T , rapidity, and centrality are reported. An enhancement of ϕ meson production is observed in the Au-going direction, while suppression is seen in the d -going direction, and no modification is observed at midrapidity relative to the yield in p + p collisions scaled by the number of binary collisions. Similar behavior was previously observed for inclusive charged hadrons and open heavy flavor indicating similar cold-nuclear-matter effects.

PACS numbers: 25.75.Dw

* Deceased

† PHENIX Co-Spokesperson: morrison@bnl.gov

‡ PHENIX Co-Spokesperson: jamie.nagle@colorado.edu

I. INTRODUCTION

Collisions of deuterons with gold nuclei ($d+Au$) are of significant interest in the study of the strongly coupled Quark Gluon Plasma (QGP) produced at the Relativistic Heavy Ion Collider (RHIC) [1, 2]. The highly asymmetric collisions of a small projectile and a large target nucleus provide a way to investigate the initial state of a nucleus-nucleus collision experimentally, potentially disentangling effects due to QGP formation from the cold-nuclear-matter effects. The latter include modification of the parton distribution functions (PDFs) in the nucleus relative to those in the nucleon [3], initial-state energy loss [4], and the so-called Cronin effect. The Cronin effect refers to the enhancement of high- p_T particle production in $p+A$ collisions relative to that in $p+p$ collisions scaled by the number of binary collisions and is often attributed to multiple scattering of the incoming parton inside the target nucleus [5–8]. In addition, results from recent $p(d)+A$ collisions at the Large Hadron Collider and RHIC suggest that long-range correlations, either present in the initial state or induced by the evolution of the medium, play an important role even in these small collision systems [7–20]. Detailed studies of particle production systematics in $d+Au$ at RHIC may inform this question [21–26].

PHENIX has measured the production of identified particles, such as π , K and p , at midrapidity in $d+Au$ and Au+Au collisions and has found intriguing similarities between the K/π and p/π ratios in peripheral Au+Au and central $d+Au$ collisions [24]. However, it was observed that the ratio of spectra in peripheral Au+Au to those in central $d+Au$ starts above one at low- p_T and trends to a constant value of ~ 0.65 for all identified particles at high p_T . One explanation for the low- p_T rise is a relative deficit of midrapidity soft particle yield in $d+Au$ collisions compared to Au+Au, which could be due to the participant asymmetry in the $d+Au$ collisions producing a rapidity shift in the peak of particle production [9]. Consequently, measuring identified particles in different regions of rapidity provides a more complete picture of $d+Au$ collisions and sheds light on the relationship between $p+p$, $d+Au$ and Au+Au. Measuring identified particle production at forward rapidity also enables access to the low- x region where nuclear PDFs (nPDFs) are not well known and where one expects parton-saturation effects to begin to manifest in modified particle production.

The yield of ϕ mesons in high energy heavy ion collisions provides key information about the QGP, as the yield is potentially sensitive to medium-induced effects such as strangeness enhancement [27], a phenomenon associated with soft particles in bulk matter which can be accessed through the measurements of ϕ meson production [28–37]. PHENIX measures ϕ meson production over a wide rapidity range and for various collision systems such as $p+p$, $d+Au$ and Au+Au. The production of ϕ mesons has already been measured in $p+p$, $d+Au$, Cu+Cu and Au+Au at midrapidity [30, 36, 38] and in $p+p$ at forward and backward rapidities [39] over a wide range in p_T .

In this paper, the production of ϕ mesons is determined at forward and backward rapidities via dimuons detected in the PHENIX muon spectrometers and at midrapidity via dielectrons detected in the PHENIX central arms. Measurements of the ϕ meson nuclear-modification factor (R_{dAu}) in $d+Au$ collisions versus rapidity and versus p_T are presented. The results presented here are based on $d+Au$ collisions at $\sqrt{s_{NN}} = 200$ GeV recorded in 2008. The luminosity used in $\phi \rightarrow \mu^+\mu^-$ analysis corresponds to 60 nb^{-1} which is equivalent to a nucleon-nucleon integrated luminosity of 24 pb^{-1} , while the luminosity used in $\phi \rightarrow e^+e^-$ analysis corresponds to 71 nb^{-1} which is equivalent to a nucleon-nucleon integrated luminosity of 28 pb^{-1} .

II. EXPERIMENT

Figure 1 shows a schematic of the PHENIX detector, which is described in detail in Ref. [40]. The detectors relevant for the analysis of the ϕ meson in the dilepton channels are the central arms, two muon spectrometers and the two beam-beam counters.

The PHENIX central arms measure particles by using drift chambers (DC) and pad chambers for the tracking and momentum measurement of charged particles, ring imaging Čerenkov detectors (RICH) for the separation of electrons up to the π meson Čerenkov radiation threshold at $5 \text{ GeV}/c$, and an electromagnetic calorimeter (EMCal) for the measurement of spatial positions and energies of photons and electrons. The EMCal comprises six sectors of lead-scintillator calorimeter and two sectors of lead-glass calorimeter.

The muon spectrometers, located at forward and backward rapidity, are shielded by absorbers composed of 19 cm of copper and 60 cm of iron. Each spectrometer comprises the muon tracker (MuTr) immersed in a radial magnetic field of integrated bending power of $0.8 \text{ T}\cdot\text{m}$, and backed by the muon identifier (MuID). The muon spectrometers subtend $1.2 < |\eta| < 2.2$ and the full azimuth. The MuTr comprises three sets of cathode strip chambers while the MuID comprises five planes of Iarocci tubes interleaved with steel absorber plates. The momentum resolution, $\delta p/p$, of particles in the analyzed momentum range is about 5%, independent of momentum and dominated by multiple scattering. Muon candidates are identified by matching tracks reconstructed in the MuTr to MuID tracks that

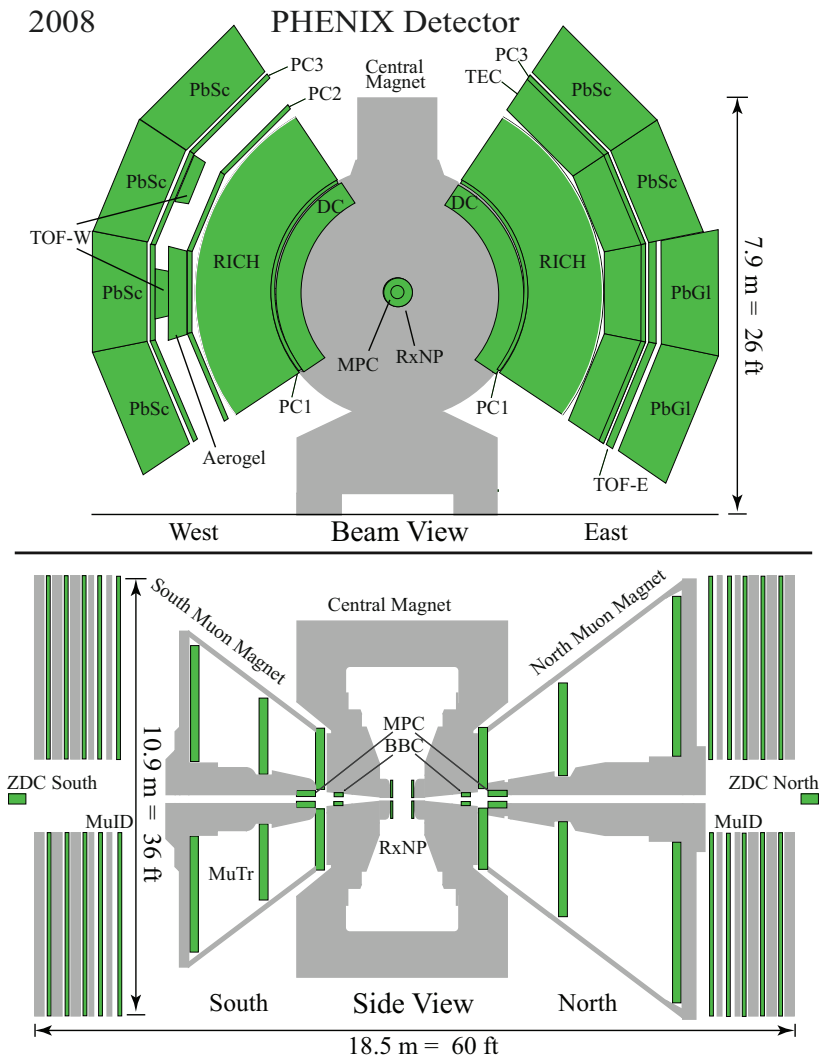


FIG. 1. (color online) A schematic side view of the PHENIX detector configuration in the 2008 data-taking period.

198 penetrate through to the last MuID plane. The minimum momentum of a muon to reach the last MuID plane is
 199 ~ 2 GeV/ c .

200 Beam-beam counters (BBC), comprising two arrays of 64 Čerenkov counters covering the pseudorapidity range
 201 $3.1 < |\eta| < 3.9$, measure the collision vertex along the beam axis (z_{vtx}) with 0.5 cm resolution in addition to providing
 202 a minimum-bias (MB) trigger.

203 III. DATA ANALYSIS

204 This section describes the details of the measurement of the ϕ meson in $\phi \rightarrow \mu^+ \mu^-$ and $\phi \rightarrow e^+ e^-$ decay channels.

205 A. $\phi \rightarrow \mu^+ \mu^-$ measurement

206 The dimuon data set for this analysis was collected in 2008 using a MB trigger that requires at least one hit in each
 207 of the BBC detectors in conjunction with the MuID Level-1 dimuon trigger. Also, at least two tracks were required
 208 to penetrate to the last layer of the MuID. The MB trigger measures $88 \pm 4\%$ of the total d +Au inelastic cross section
 209 of 2260 mb [21].

210 A set of cuts was employed to select good muon candidates and improve the signal to background ratio. Event

211 selection requires the BBC collision z vertex to be reconstructed within ± 30 cm of the center of the interaction region
 212 along the beam axis. The MuTr tracks are matched to the MuID tracks at the first MuID layer in both position and
 213 angle. The track is required to have at least 8 of 10 possible hits in the MuID.

214 The invariant mass distribution is formed by combining muon candidate tracks of opposite charge. In addition to
 215 low mass vector mesons, the invariant mass spectra in the region of interest contain uncorrelated and correlated back-
 216 grounds. The uncorrelated backgrounds arise from random combinatoric associations of unrelated muon candidates
 217 while the correlated backgrounds arise from open charm decay (e.g., $D\bar{D}$ where both mesons decay semileptonically
 218 to muons), open bottom decay, η and ω Dalitz decays and from the Drell-Yan process. The correlated background
 219 is much smaller than the uncorrelated background for all centralities. It is also established from simulation that the
 220 background is dominated by the uncorrelated contribution from decays, such as $K, \pi \rightarrow \mu\nu$, that occur in front of
 221 and inside the absorber. A smaller contribution to the background comes from hadron decays in the muon tracker
 222 volume. When combined into track pairs, these pairs produce a broad distribution of invariant masses and also a
 223 broad distribution of χ^2_{vtx} , the parameter resulting from fitting the two muon tracks with the BBC measured event
 224 vertex position. This procedure separates the foreground and background spectra by applying a cut of $\chi^2_{\text{vtx}} < 4.0$
 225 to extract foreground spectra and a cut of $\chi^2_{\text{vtx}} > 4.0$ to extract background spectra. The cut value, $\chi^2_{\text{vtx,cut}} = 4.0$,
 226 is selected such that it retains as much of the signal as possible within the foreground, while still allowing sufficient
 227 statistics in the background sample. This procedure is described in detail in Ref. [39].

228 To extract the ϕ meson signal, the background pairs are subtracted from the foreground pairs. Because the pairs
 229 with $\chi^2_{\text{vtx}} > 4.0$ represent only the uncorrelated part of the background the shape of their mass distribution is
 230 slightly altered to account for the contribution of correlated pairs, which have much smaller contribution according
 231 to simulation results. This is done by fitting a fourth order polynomial to the ratio of the foreground to background
 232 distributions in the nonresonance region ($0.3 < M_{\mu^+\mu^-} < 0.5 \text{ GeV}/c^2$ and $1.5 < M_{\mu^+\mu^-} < 2.5 \text{ GeV}/c^2$). The
 233 background distribution is then multiplied by the polynomial in the entire mass range. Figure 2 shows the resulting
 234 foreground and renormalized background distributions.

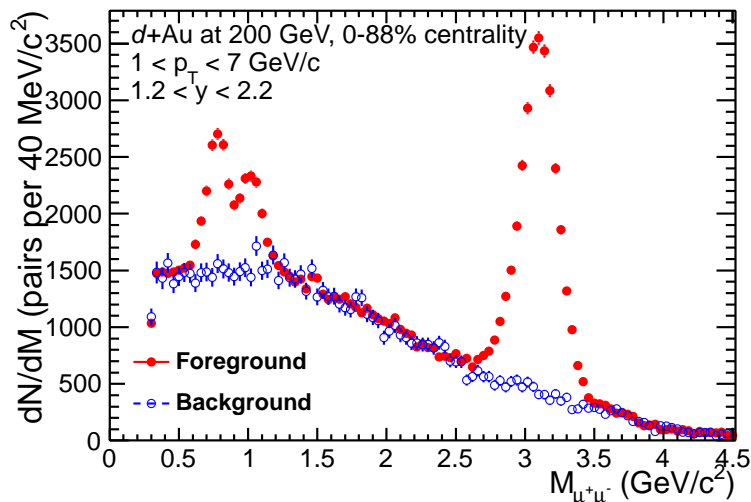


FIG. 2. (color online) The unlike-sign dimuon invariant mass spectrum (solid red points) and the renormalized background spectrum (open blue circles).

235 In the mass range $0.3 < M_{\mu^+\mu^-} < 2.5 \text{ GeV}/c^2$, the resulting distribution after subtraction has contributions from
 236 three mesons: ω , ρ , and ϕ mesons. The distribution is fitted with the sum of two Gaussian functions and the Breit-
 237 Wigner function convoluted with a Gaussian. The Gaussian functions are used to fit the ω and ϕ mesons while the
 238 Breit-Wigner convoluted with a Gaussian is used to fit the ρ meson. Figure 3 shows the results.

239 The parameters of the fit are fixed to the world average values of the masses and widths of the three mesons [41]
 240 and the widths of the Gaussian distributions, which account for the detector mass resolution, are constrained by the
 241 values obtained from the simulation. The ϕ meson mass resolution is $\sim 85 \text{ MeV}/c^2$. Because the invariant mass peak
 242 of the ϕ meson is partly resolved in the plot, while ω and ρ meson peaks cannot be resolved, only an estimate of the
 243 combined yield of these two mesons is allowed. In the fit, the ratio of the ω and ρ mesons, N_{ρ}/N_{ω} , is set to 0.58,
 244 derived as the ratio of their corresponding production cross sections, $\sigma_{\rho}/\sigma_{\omega} = 1.15 \pm 0.15$, consistent with values
 245 found in jet fragmentation [42], multiplied by the ratio of their branching ratios [41].

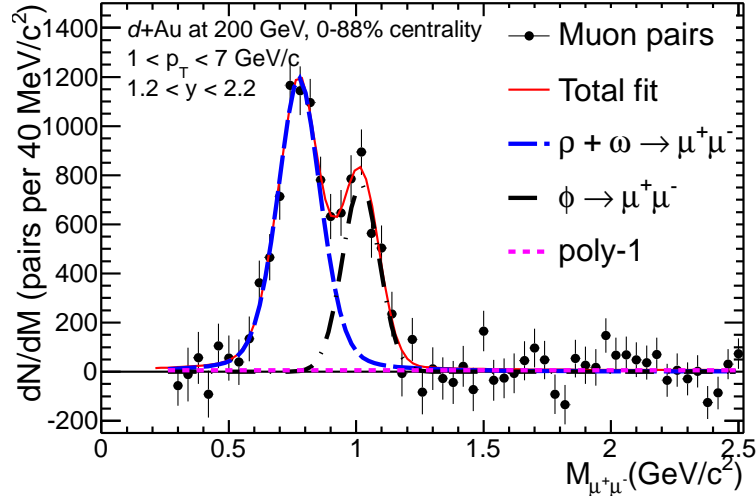


FIG. 3. (color online) The fitted unlike-sign dimuon spectra after background subtraction.

246 The yield extraction is performed in bins of p_T over the range $1 < p_T < 7$ GeV/ c for the rapidities $1.2 < |y| < 2.2$,
 247 in bins of y for the p_T range $1 < p_T < 7$ GeV/ c , and in different centrality classes.

248 The acceptance and reconstruction efficiency ($A\varepsilon_{\text{rec}}$) of the muon spectrometers, including the MuID trigger effi-
 249 ciency, is determined by passing PYTHIA 6.421 (default parameters) [43] generated ϕ mesons through a full GEANT [44]
 250 simulation of the PHENIX detector. The PYTHIA simulation output is embedded into real $d+Au$ data events and
 251 then reconstructed in the same manner as data. Identical cuts to those used in the data analysis are applied to this
 252 embedded simulation.

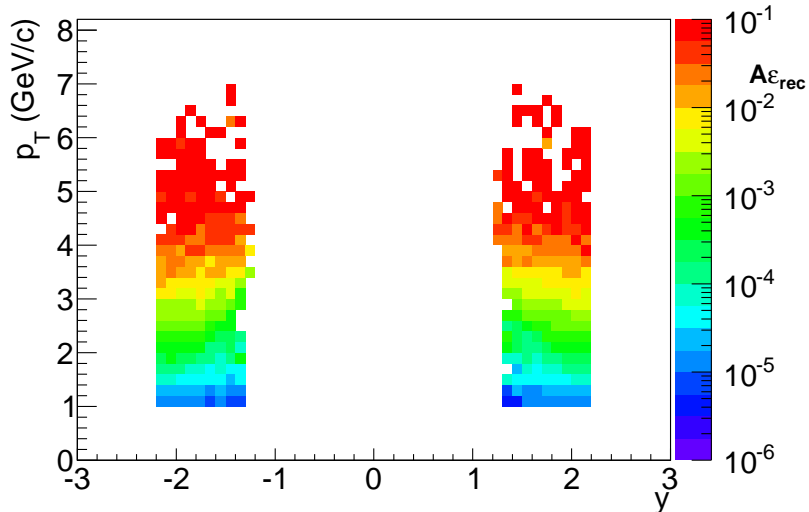


FIG. 4. (color online) The $A\varepsilon_{\text{rec}}$ as a function of rapidity (x -axis) and p_T (y -axis) for ϕ mesons.

253 Figure 4 shows the $A\varepsilon_{\text{rec}}$ as a function of p_T and rapidity for ϕ mesons. The $A\varepsilon_{\text{rec}}$ reaches a few percent at high- p_T
 254 and rapidly decreases at low momentum limiting this study to $p_T > 1$ GeV/ c .

B. $\phi \rightarrow e^+e^-$ measurement

The dielectron data set for this analysis was recorded in 2008 using a MB trigger that required at least one hit in each of the BBC detectors with an ERT (EMCal-RICH trigger). The ERT requires a minimum energy deposit of 0.6 and 0.8 GeV/c in a tile of 2×2 EMCal towers matched to a hit in the RICH. The trigger efficiencies are described in detail in Ref. [45].

A set of quality assurance cuts is applied to the data to select good electron candidates and improve the signal to background ratio. Event selection requires the BBC collision z vertex to be reconstructed within ± 30 cm of the center of the interaction region along the beam direction. Charged tracks are reconstructed using the DC and pad chambers and requiring $p_T > 0.2$ GeV/c. Electrons are identified mainly by the RICH detector. Furthermore, an electron candidate is required to have a good match to a cluster in the EMCal, and the energy, E , of the cluster must satisfy the requirement $E/p > 0.5$, where p is the momentum measured by the DCs. The RICH and EMCal combined provide an e/π rejection factor of order 10^4 .

Electrons and positrons reconstructed in an event are combined into pairs. The resulting mass spectrum contains both the signal and an inherent background. The uncorrelated part of the background is estimated via an event-mixing technique [46], which combines electrons from different events within the same centrality and vertex class. To extract the ϕ meson raw yield, the subtracted mass spectrum is fitted by a function consisting of several contributions. The ϕ and ω meson peaks are approximated by a Breit-Wigner distribution convolved with a Gaussian distribution. Parameters of the Breit-Wigner part are set to the global averaged values [41] and the width of the Gaussian part is to account for the detector mass resolution. Because the production ratio of ρ meson to ω meson is assumed to be 1.15, their ratio in the fit is given by the ratio of their branching ratios to e^+e^- in vacuum. The ϕ meson yield is then extracted by summing up the bin contents in a $\pm 3\sigma$ window, where σ is extracted from the fit, and subtracting the background determined by integrating the polynomial over the same window.

Figure 5 shows an example of the fit to the mixed event subtracted mass spectrum. The mixed events were normalized in the mass range between 0.7 to 1.5 GeV/c². The stability of the results was checked by varying the normalization region, and the difference was included in the systematic errors. The ratio of real to normalized mixed events was found to be flat in the region of interest for this analysis indicating the validity of the normalization. Complete details describing the estimation of the systematic uncertainty on the raw yield extraction by varying the background normalization, fitting functions, range and counting method can be found in Ref. [45].

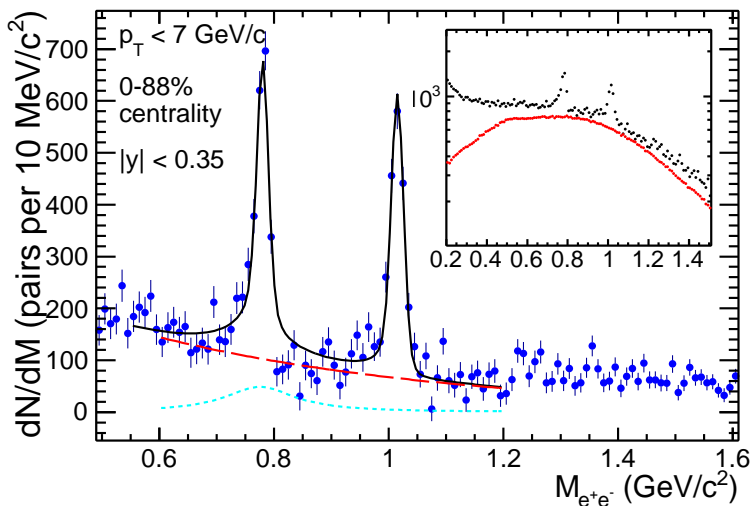


FIG. 5. (color online) p_T -integrated unlike-sign e^+e^- mass spectrum measured by the PHENIX central arms after subtracting the uncorrelated combinatorial background in the minimum-bias $d+Au$ collisions. The dotted-line shows the ρ meson contribution and the dashed line is the polynomial background, which describes the residual correlated background. The insert shows the raw spectrum before subtraction, overlaid with the normalized combinatorial background, which is estimated using the mixed-event technique.

The detector acceptance and reconstruction efficiency, as well as trigger efficiency were determined using a GEANT [44] based simulation of the PHENIX detector that tuned the detector response to a set of characteristics (dead and hot channel maps, gains, noise, etc) that described the performance of each detector subsystem. The

286 $\phi \rightarrow e^+e^-$ decays were generated with a realistic p_T distribution of ϕ mesons, within $|y| < 0.5$ in rapidity, and in full
 287 azimuth. The simulated ϕ meson mean and width of the invariant mass peak were verified to match the measured
 288 values in real data at all p_T . More details are given in Ref. [38].

289 C. Calculation of invariant yields and nuclear-modification factors

290 The dilepton ϕ meson invariant yield in a given rapidity, p_T , and centrality bin is

$$\frac{B_{ll}}{2\pi p_T} \frac{d^2 N}{dy dp_T} = \frac{1}{2\pi p_T} \frac{1}{\Delta y \Delta p_T} \frac{c N_\phi}{\varepsilon_{\text{tot}} N_{\text{evt}}}, \quad (1)$$

291 where B_{ll} is the $\phi \rightarrow l^+l^-$ branching ratio, N_ϕ is the measured ϕ meson yield, N_{evt} is the number of sampled MB
 292 events in the given centrality bin, Δy is the width of the rapidity bin, Δp_T is the width of the p_T bin, , and c is the
 293 BBC bias correction factor [21, 47]. ε_{tot} includes trigger efficiencies, acceptance and reconstruction efficiency [45, 48].
 294 The data points are corrected to account for the finite width of the analyzed p_T bins [49].

295 To gain insight into nuclear medium effects and particle production mechanisms in d +Au collisions, the ratio of the
 296 ϕ meson yields in d +Au collisions to p + p collisions scaled by the number of nucleon-nucleon collisions in the d +Au
 297 system, N_{coll} [21], is calculated as:

$$R_{d\text{Au}} = \frac{d^2 N_{d\text{Au}}/dy dp_T}{N_{\text{coll}} \times d^2 N_{pp}/dy dp_T}, \quad (2)$$

298 where $d^2 N_{d\text{Au}}/dy dp_T$ is the per-event yield of particle production in d +Au collisions and $d^2 N_{pp}/dy dp_T$ is the
 299 per-event yield of the same process in p + p collisions. The p + p invariant yield used in the $R_{d\text{Au}}$ calculation for
 300 the $\mu^+\mu^-$ decay channel is the p + p differential cross section from Ref. [39] divided by the p + p total cross section,
 301 42.2 mb. The measured p + p differential cross sections for e^+e^- and K^+K^- decay channels are consistent [38] and the
 302 p + p reference used in the e^+e^- $R_{d\text{Au}}$ calculations is extracted from a Tsallis function fit of the combined e^+e^- and
 303 K^+K^- spectra.

304 D. Systematic uncertainties

305 The systematic uncertainties associated with the measured invariant yields and nuclear modification factors can
 306 be divided into three categories based upon the effect each source has on the measured results. All uncertainties
 307 are reported as standard deviations. Type-A: point-to-point uncorrelated uncertainties that allow the data points to
 308 move independently with respect to one another and are added in quadrature with statistical uncertainties. Type-B:
 309 point-to-point correlated uncertainties that allow the data points to move coherently within the quoted range. Type-
 310 C: correlated uncertainties that allow the data points to move together by a common multiplicative factor, a global
 311 uncertainty.

312 At forward and backward rapidities, a 5% type-A uncertainty is assigned to signal extraction, which corresponds to
 313 the average variation between the results from the different yield extraction fits. Type-B uncertainties, point-to-point
 314 correlated uncertainties to some degree in p_T , include a 4% uncertainty from MuID tube efficiency and 2% from
 315 MuTr overall efficiency. An 8% uncertainty on the yield is assigned to account for a 2% absolute momentum scale
 316 uncertainty, which was estimated by measuring the J/ψ mass.

317 A 9% (8%) uncertainty is assigned to the $-2.2 < y < -1.2$ ($1.2 < y < 2.2$) rapidity bins due to the uncertainties in
 318 the $A\varepsilon_{\text{rec}}$ determination method itself. The $A\varepsilon_{\text{rec}}$ at the lowest p_T bin is small and sensitive to variations in the slope
 319 of the input p_T distribution which affects the differential cross section calculations at this p_T bin. To understand
 320 this effect, the p_T dependent cross section is fitted by three commonly used fit functions (Hagedorn [50], Kaplan [51],
 321 and Tsallis [38]) over the p_T range, $2 < p_T < 7$ GeV/ c , and the fitted functions are extrapolated to the lowest p_T
 322 bin, $1 < p_T < 2$ GeV/ c . The differences between the values extracted from these fits and the measured one at
 323 the lowest p_T bin is within 8%, hence an additional 8% systematic uncertainty is assigned to the lowest p_T bin to
 324 account for these differences. For the p_T integrated and rapidity dependent invariant yields the 8% uncertainty is
 325 assigned to all data bins. Type-B systematic uncertainties are added in quadrature and are shown as boxes. Finally,
 326 an overall normalization uncertainty of 10% (0.1%–5.8%) for p + p (d +Au) is assigned to the BBC bias correction (c)
 327 uncertainties and are labeled as type-C [23]. The BBC bias correction uncertainties for d +Au vary with centrality
 328 and are considered as type-B for centrality dependent spectra.

329 For the nuclear modification factor, the type-A systematic uncertainties arise from the quadratic sum of type-A
 330 systematic uncertainty in p + p and d +Au invariant yields [39]. Systematic uncertainties including MuID and MuTr

TABLE I. Systematic uncertainties included in the invariant yield and the nuclear modification factor calculations at forward and backward rapidities. As explained in the text, there is an 8% type-B systematic uncertainty due to small acceptance that impacts the low- p_T region only which is not listed below.

Source	Value (%)	Type
Signal extraction	5	A
MuID efficiency	4	B
MuTr efficiency	2	B
$A\varepsilon_{\text{rec}}$ [north/south]	8 / 9	B
Absolute momentum scale	8	B
Total Type-B	13	B
BBC bias correction for $p+p$ ($d+\text{Au}$)	10 (0.1–5.8)	C
N_{coll}	5–7	C

TABLE II. Systematic uncertainties included in the invariant yield and the nuclear modification factor calculations at midrapidity.

Source	Value (%)	Type
Signal extraction	8–15	A
ERT trigger efficiency	1–7	B
Acceptance correction	7	B
Electron ID	9	B
Absolute momentum scale	1–5	B
Quadratic sum of (B)	11–14	B
BBC bias correction for $p+p$ ($d+\text{Au}$)	10 (0.1–5.8)	C
N_{coll}	5–7	C

331 efficiencies and absolute momentum scale are the same between the $d+\text{Au}$ and $p+p$ invariant yields and cancel out.
 332 A 9% (7%) systematic uncertainty in the $A\varepsilon_{\text{rec}}$ at $-2.2 < y < -1.2$ ($1.2 < y < 2.2$), that is carried over from $p+p$,
 333 is added in quadrature to type-B systematic uncertainties listed in Table I. The acceptance limitation at the lowest
 334 p_T bin is the same between $d+\text{Au}$ and $p+p$ data because it is collected using the same detector and the associated
 335 type-B systematic uncertainty cancels out. Type-C systematic uncertainties for the nuclear modification factor are
 336 the quadratic sum of the type-C systematic uncertainties for the invariant yields of $p+p$ and $d+\text{Au}$ collisions and the
 337 uncertainty associated with N_{coll} . The systematic uncertainties are listed in Table I.

338 At midrapidity, the main contribution to the systematic uncertainties of type-A is the uncertainty associated with
 339 the raw yield extraction, 8%–15%. This uncertainty is calculated by varying the background normalization, fitting
 340 functions, range, and counting methods. Type-B systematic uncertainties, point-to-point correlated uncertainties in
 341 p_T , include uncertainties in the ERT trigger efficiency (1%–7%) and electron identification (9%), which are estimated
 342 by varying the analysis cuts. The acceptance correction uncertainty is 7% and the momentum scale uncertainty is
 343 1%–5%. An overall normalization uncertainty, type-C, was assigned for the $p+p$ ($d+\text{Au}$) BBC bias correction, which
 344 amounts to 10% (0.1%–5.8%).

345 For the nuclear-modification factor, the electron identification and branching ratio uncertainties are the same
 346 between $p+p$ and $d+\text{Au}$ and cancel out. As for the rest of the systematic uncertainties, the uncertainties for each
 347 type are added in quadrature between $p+p$ and $d+\text{Au}$. Additionally, the N_{coll} uncertainty is added in quadrature to
 348 the rest of type-C uncertainties. The systematic uncertainties are listed in Table II.

349 IV. RESULTS

350 Figure 6 shows the ϕ meson invariant yields in $d+\text{Au}$ and $p+p$ as a function of p_T in the Au-going direction
 351 $-2.2 < y < -1.2$, in the d -going direction $1.2 < y < 2.2$, and at midrapidity $|y| < 0.35$. The invariant yields measured
 352 at forward and backward rapidities for all centralities are significantly different from each other. At midrapidity, the
 353 magnitude of the invariant yield is close to
 354 that of the backward rapidity, in contrast to what was observed in $p+p$ collisions [38] where the forward and backward

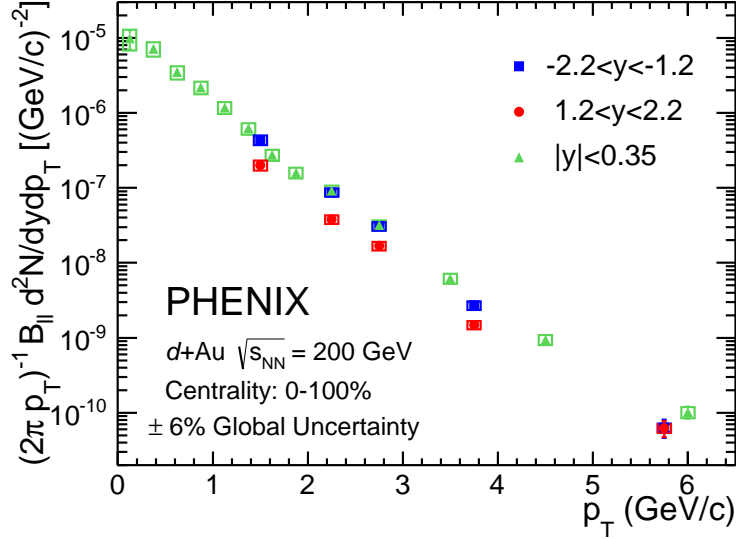


FIG. 6. (color online) ϕ meson invariant yields as a function of p_T in the Au-going direction (solid blue squares) and in the d -going direction (solid red points). The ϕ meson invariant yields at midrapidity are shown as solid green triangles. The vertical bars represent the statistical uncertainties and the boxes represent type-B systematic uncertainties. The $\pm 6\%$ global uncertainty is the associated type-C uncertainty.

355 rapidities have the same invariant yields and both are smaller than the midrapidity invariant yield.

356 Figure 7 shows the invariant yields as a function of p_T for the different centrality intervals measured in $p+p$ and
 357 $d+Au$ collisions. The $d+Au$ data are presented in different centrality classes: 0%–20%, 20%–40%, 40%–60%, and
 358 60%–88%, which are determined using the BBC over the pseudorapidity range $3.1 < |\eta| < 3.9$, for the $1.2 < |y| < 2.2$
 359 and $|y| < 0.35$ regions. The three panels describe the three rapidity regions. The same centrality definition is used as
 360 in Ref. [47]. The wide rapidity coverage of the full PHENIX detector over an extended p_T range is demonstrated.

361 Figure 8 shows the R_{dAu} for ϕ mesons measured in all centralities as a function of p_T for forward and backward
 362 rapidities and at midrapidity, also compared with R_{dAu} measured in the $\phi \rightarrow K^+K^-$ decay channel [36]. The ϕ
 363 meson R_{dAu} behavior measured in the three different rapidity regions is not the same. In the Au-going direction,
 364 the R_{dAu} is consistent with unity at the lowest measured p_T and increases to $R_{dAu} \sim 2$ at $p_T = 2.7$ GeV/c. It then
 365 decreases to unity at the highest measured p_T . In the d -going direction strong suppression is observed at the lowest
 366 measured p_T and then the R_{dAu} increases to unity at higher p_T . At midrapidity, where the measurement starts at
 367 $p_T = 0$, the yield of the ϕ meson is suppressed below 1 GeV/c and R_{dAu} is consistent with unity above that. The
 368 R_{dAu} measured in the $\phi \rightarrow K^+K^-$ channel agrees with the measurement of $\phi \rightarrow e^+e^-$ within uncertainties in the p_T
 369 region where the measurements overlap. The enhanced yield observed in the Au-going direction at intermediate p_T
 370 is characteristic of the Cronin effect [5]: enhancement of high p_T particle production in $d+Au$ collisions relative to
 371 scaled $p+p$ collisions with a corresponding depletion at low p_T . The ϕ enhancement in the Au-going direction and
 372 the suppression in the d -going direction are consistent with what is observed by ALICE in $p+Pb$ collisions at $\sqrt{s_{NN}}$
 373 = 5.02 TeV in $-4.46 < y < -2.96$ and $2.03 < y < 3.53$ [53].

374 Figure 9 shows the R_{dAu} of the ϕ meson as a function of rapidity, summed over the p_T range $1 < p_T < 7$ GeV/c and
 375 integrated over all centralities. The R_{dAu} is enhanced in the Au-going direction, shows no modification at midrapidity
 376 and is suppressed in the d -going direction.

377 Figure 10 shows that the ϕ meson nuclear modification factor, measured as a function of rapidity, is consistent with
 378 that of leptons coming from decays of heavy flavor particles [22, 26]. This similarity is interesting given that heavy
 379 flavor quark production is expected to be dominated by hard processes over the accessed p_T range. In contrast, one
 380 expects a significant contribution to ϕ meson production from soft processes, particularly at low p_T where the yield
 381 is dominant. This backward/forward enhancement/suppression in $d+Au$ collisions is also observed in $d+Au$ charged
 382 hadron density results measured by PHOBOS [10]. The charged hadron result is often considered as a rapidity shift
 383 in the Au-going direction via soft processes.

384 Figure 10 also shows the J/ψ R_{dAu} [52]. In the case of the J/ψ , the relative R_{dAu} modification as a function of
 385 rapidity is similar to that of the ϕ meson and heavy flavor decay leptons. However, the J/ψ suffers from additional
 386 suppression at backward and midrapidity, which could be due to a larger break up cross section or effects in the

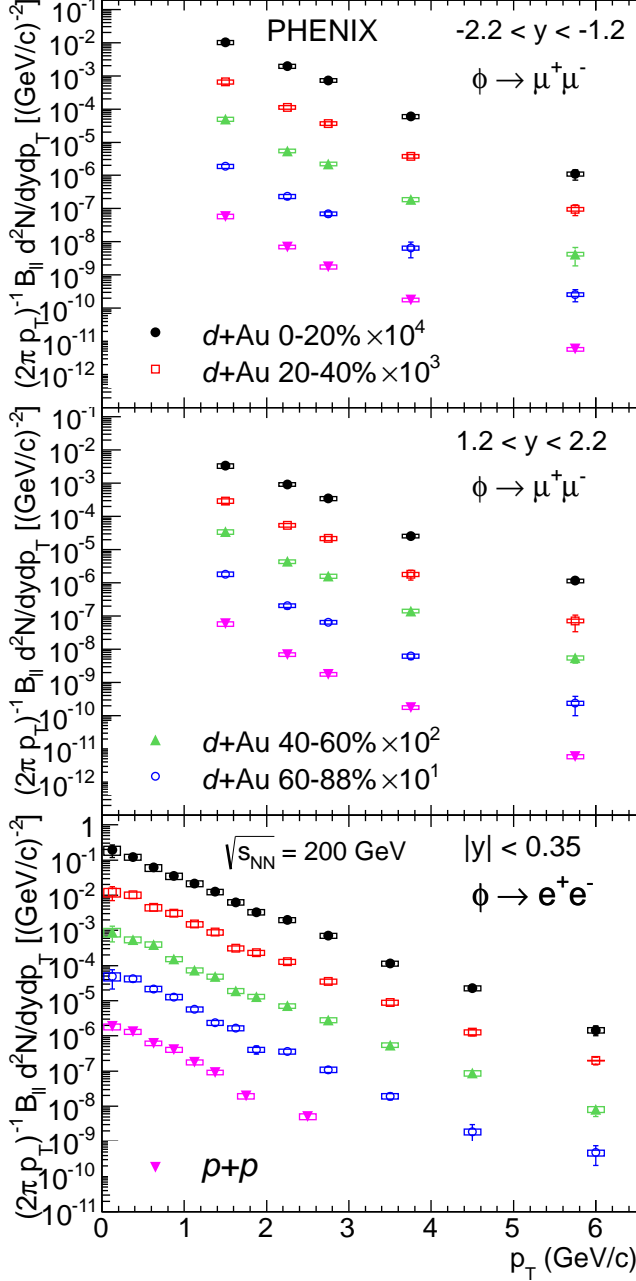


FIG. 7. (color online) Invariant p_T spectra of the ϕ meson for different centrality classes in $d+Au$ and $p+p$ collisions at $\sqrt{s_{NN}} = 200$ GeV [39]. The vertical bars represent the statistical uncertainties and the boxes represent type-B systematic uncertainties. Type-C systematic uncertainties are 0.1%–5.8% for $d+Au$ invariant yields and 10% for $p+p$ invariant yields. The spectra are scaled by arbitrary factors for clarity.

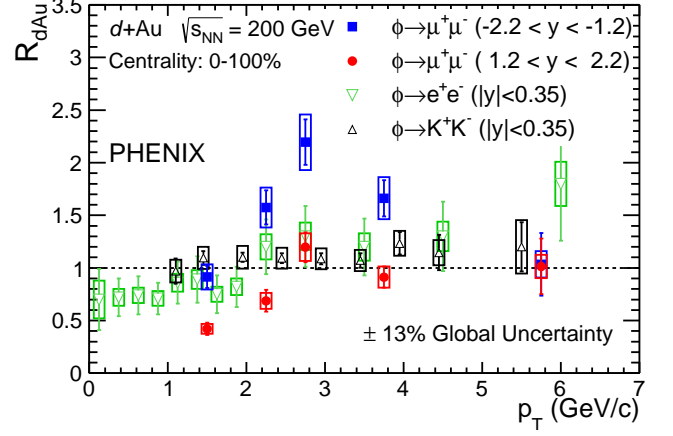


FIG. 8. (color online) The ϕ meson nuclear-modification factor, R_{dAu} , as a function of p_T . The solid blue squares indicate the Au-going direction and the solid red circles indicate the d -going direction. The upright black triangles are for $\phi \rightarrow K^+K^-$ at midrapidity [36] while the inverted triangles are for $\phi \rightarrow e^+e^-$. The vertical bars represent the statistical uncertainties and the boxes represent type-B systematic uncertainties. The $\pm 13\%$ global uncertainty is the associated type-C uncertainty.

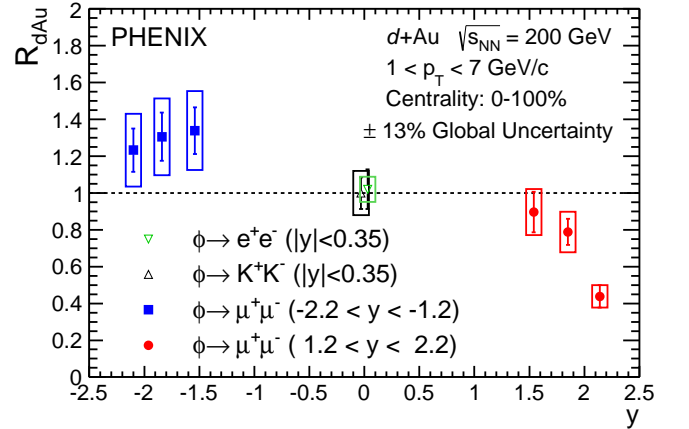


FIG. 9. (color online) The ϕ meson nuclear modification factor, R_{dAu} , as a function of rapidity. The solid blue squares indicate the Au-going direction while the d -going direction is shown in solid red circles. At midrapidity, the upright black triangles are for $\phi \rightarrow K^+K^-$ [36] while the inverted triangles are for $\phi \rightarrow e^+e^-$. The midrapidity points are slightly displaced from zero for clarity. The vertical bars represent the statistical uncertainties and the boxes represent type-B systematic uncertainties. The $\pm 13\%$ global uncertainty is the associated type-C uncertainty.

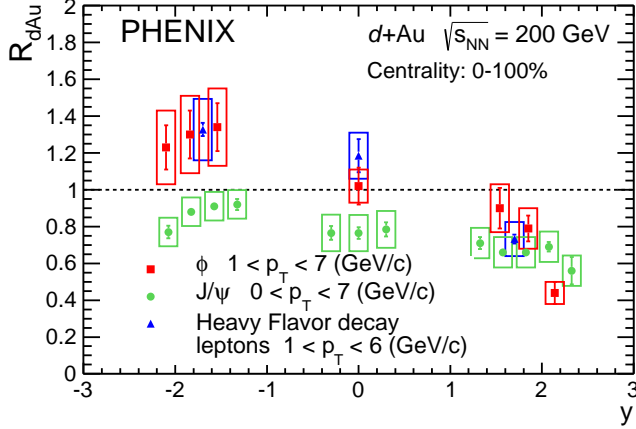


FIG. 10. (color online) J/ψ [52] (full green circles), heavy flavor decay leptons [22, 26] (full blue triangles) and ϕ meson (full red squares) nuclear modification factors, R_{dAu} , as a function of rapidity. The vertical bars represent the statistical uncertainties and the boxes represent type-B systematic uncertainties. The type-C systematic uncertainties associated with heavy-flavor and J/ψ meson measurements are 10% and 8%, respectively.

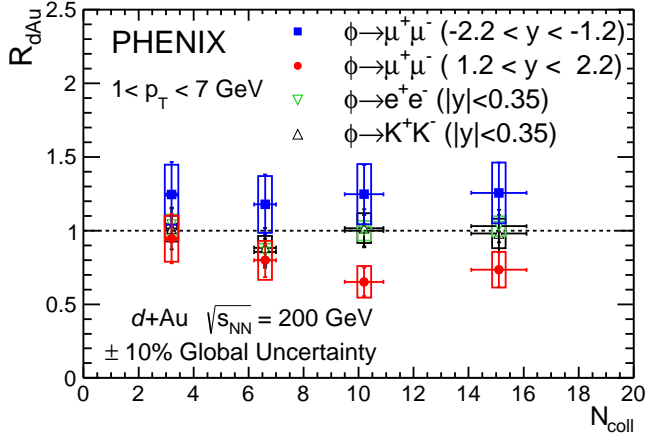


FIG. 11. (color online) The ϕ meson nuclear modification factor, R_{dAu} , as a function of N_{coll} . The solid blue squares indicate the Au-going direction while the d -going direction is shown in solid red circles. At midrapidity, the upright black triangles are for $\phi \rightarrow K^+K^-$ [36] while the inverted triangles are for $\phi \rightarrow e^+e^-$. The vertical bars represent the statistical uncertainties and the boxes represent type-B systematic uncertainties. The $\pm 10\%$ global uncertainty is the associated type-C uncertainty.

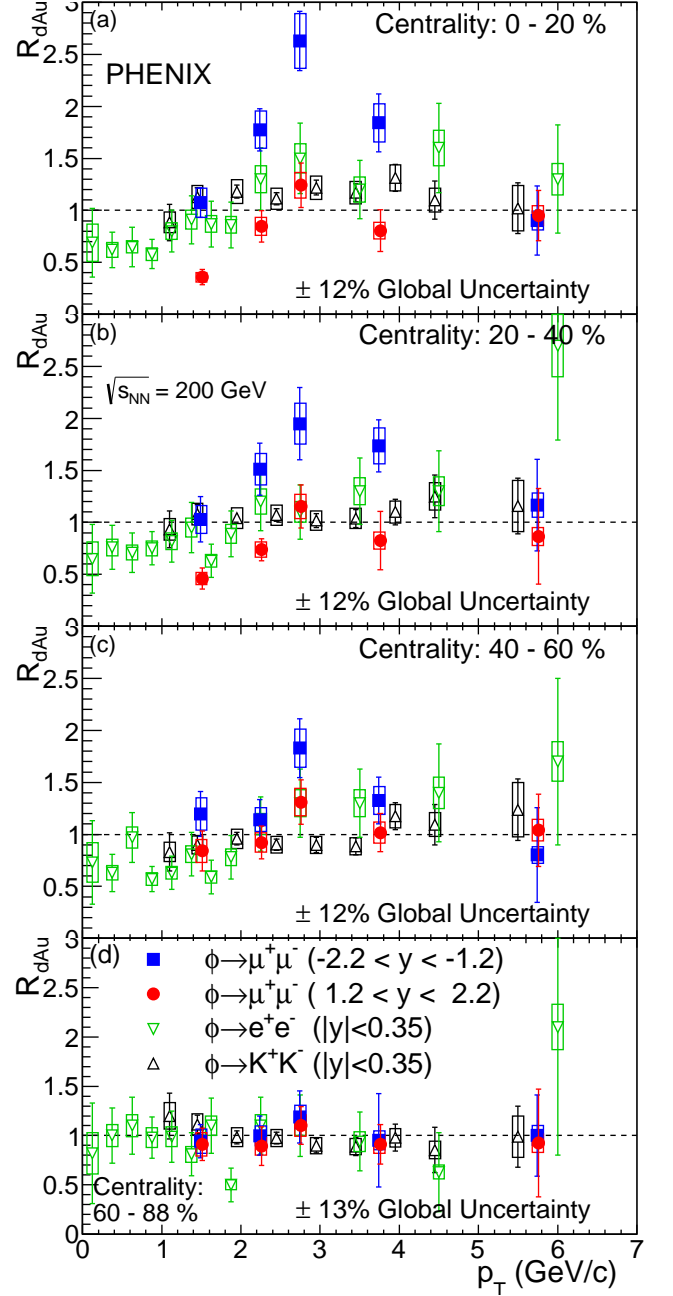


FIG. 12. (color online) The ϕ meson R_{dAu} as a function of p_T for the centralities (a) 0%–20%, (b) 20%–40%, (c) 40%–60%, and (d) 60%–88% in the Au-going direction (solid blue squares) and the d -going direction (solid red circles). At midrapidity, the upright black triangles are from $\phi \rightarrow K^+K^-$ [36] while the upside down triangles are from $\phi \rightarrow e^+e^-$. The vertical bars represent the statistical uncertainties and the boxes represent type-B systematic uncertainties. The $\pm 12\%$ – 13% global uncertainty is the associated type-C uncertainty.

387 higher-energy-density backward-rapidity region.

388 At midrapidity, PHENIX measured the nuclear-modification factors of protons and of several mesons from the light
 389 (π) meson up to the ϕ meson with a mass similar to that of protons. The results show no significant dependence
 390 of R_{dAu} on the mass of the particle [24], whereas the measurements reveal a significant dependence of R_{dAu} on the
 391 number of valence quarks. All mesons show no or very small enhancement in comparison to protons in the low to
 392 medium p_T region.

393 Figure 11 shows the R_{dAu} integrated over the p_T range $1 < p_T < 7$ GeV/ c as a function of centrality for three
 394 rapidity intervals: $-2.2 < y < -1.2$, $1.2 < y < 2.2$ and $|y| < 0.35$. The R_{dAu} is integrated over the p_T range
 395 $1 < p_T < 7$ GeV/ c and the rapidity ranges $-2.2 < y < -1.2$, $1.2 < y < 2.2$ and $|y| < 0.35$. In the Au-going direction,
 396 the R_{dAu} shows an indication of enhancement with N_{coll} and in the d -going direction shows a strong suppression at
 397 high N_{coll} . At midrapidity, the R_{dAu} for ϕ mesons reconstructed in e^+e^- is consistent with unity at all centralities.
 398 This is also consistent with the measurement done in the K^+K^- decay channel.

399 Figure 12 shows R_{dAu} as a function of p_T in different d +Au centrality classes for three rapidity regions covered by
 400 the PHENIX detector: backward, mid, and forward rapidities. In the most peripheral collisions (60%–88%), shown
 401 in the lowest panel of the figure, the nuclear-modification factor measured in all three rapidity regions is consistent
 402 with unity at all measured p_T . In the more central collisions the R_{dAu} remains at unity only in the midrapidity region
 403 for p_T above 1 GeV/ c . This is consistent between the measurements done in the e^+e^- and in the K^+K^- decay
 404 channels. In the Au-going direction, the R_{dAu} reaches a maximum at p_T close to 2.7 GeV/ c with an amplitude that
 405 grows towards more central collisions. At higher p_T the R_{dAu} diminishes, approaching unity in all measured centrality
 406 classes. In the d -going direction, all points above 2.7 GeV/ c are consistent with unity. Below $p_T = 2.7$ GeV/ c Fig. 12
 407 shows $R_{dAu} < 1$, with more suppression in the most central collisions compared to other centralities.

408 The enhancement at backward rapidity is consistent with nuclear p_T broadening at moderate p_T and gluon anti-
 409 shadowing, while the suppression at forward rapidity may suggest gluon shadowing and/or partonic energy loss. The
 410 R_{dAu} enhancement (suppression) at backward (forward) rapidity in the most central collisions decreases gradually
 411 from central to peripheral collisions where for the most peripheral collisions R_{dAu} shows no overall modification.
 412 Whether the ϕ meson is dominated by soft or hard processes remains an open question.

413 V. SUMMARY AND CONCLUSIONS

414 PHENIX has measured the production of ϕ mesons in $d+Au$ collisions at $\sqrt{s_{NN}} = 200$ GeV via their decay to
 415 dimuons and dielectrons. The ϕ meson is measured in the forward, d -going direction, $1.2 < y < 2.2$ in the p_T range
 416 from 1 to 7 GeV/ c , at midrapidity $|y| < 0.35$ in the p_T range below 7 GeV/ c , and in the backward, the Au-going
 417 direction, $-2.2 < y < -1.2$ in the p_T range from 1 to 7 GeV/ c .

418 The measurements reveal that the ϕ meson yields in $d+Au$ compared to binary collision scaled $p+p$ at $p_T > 2$ GeV/ c
 419 are suppressed in the d -going direction and enhanced in the Au-going direction. The yield measured at midrapidity
 420 is consistent with binary collision scaled $p+p$. No significant modification of ϕ meson production is observed in
 421 the most peripheral $d+Au$ collisions. With centrality increasing from semi-peripheral events to central the R_{dAu}
 422 shows more pronounced suppression in the d -going and more increasing enhancement in Au-going direction. In that
 423 rapidity region, the R_{dAu} has a p_T dependence, which is characteristic of a Cronin-type effect. A similar enhancement
 424 (suppression) was observed by ALICE in $p+Pb$ collisions at $\sqrt{s_{NN}} = 5.02$ TeV [53]. The rapidity dependence of
 425 the R_{dAu} in ϕ -meson production is similar to the open heavy flavor modification [26] which may indicate a general
 426 rapidity shift compared to the symmetric system and/or similar cold-nuclear matter effects are present in both the ϕ
 427 meson and open heavy-flavor production.

428 ACKNOWLEDGMENTS

429 We thank the staff of the Collider-Accelerator and Physics Departments at Brookhaven National Laboratory and
 430 the staff of the other PHENIX participating institutions for their vital contributions. We acknowledge support from
 431 the Office of Nuclear Physics in the Office of Science of the Department of Energy, the National Science Foundation,
 432 Abilene Christian University Research Council, Research Foundation of SUNY, and Dean of the College of Arts
 433 and Sciences, Vanderbilt University (U.S.A), Ministry of Education, Culture, Sports, Science, and Technology and
 434 the Japan Society for the Promotion of Science (Japan), Conselho Nacional de Desenvolvimento Científico e Tec-
 435 nológico and Fundação de Amparo à Pesquisa do Estado de São Paulo (Brazil), Natural Science Foundation of China
 436 (P. R. China), Ministry of Science, Education, and Sports (Croatia), Ministry of Education, Youth and Sports (Czech
 437 Republic), Centre National de la Recherche Scientifique, Commissariat à l'Énergie Atomique, and Institut National de
 438 Physique Nucléaire et de Physique des Particules (France), Bundesministerium für Bildung und Forschung, Deutscher
 439 Akademischer Austausch Dienst, and Alexander von Humboldt Stiftung (Germany), National Science Fund, OTKA,
 440 Károly Róbert University College, and the Ch. Simonyi Fund (Hungary), Department of Atomic Energy and Depart-
 441 ment of Science and Technology (India), Israel Science Foundation (Israel), Basic Science Research Program through
 442 NRF of the Ministry of Education (Korea), Physics Department, Lahore University of Management Sciences (Pak-
 443 istan), Ministry of Education and Science, Russian Academy of Sciences, Federal Agency of Atomic Energy (Russia),
 444 VR and Wallenberg Foundation (Sweden), the U.S. Civilian Research and Development Foundation for the Indepen-
 445 dent States of the Former Soviet Union, the Hungarian American Enterprise Scholarship Fund, and the US-Israel
 446 Binational Science Foundation.

447 APPENDIX

448 Tables III–VI show the numerical values of the measured invariant yields and R_{dAu} that are plotted in Figs. 6–12.
 449 As noted in each caption, the first uncertainty is statistical and the second is type-B systematic.

TABLE III. Invariant yields of ϕ meson production as a function of p_T at different d +Au centrality classes. The first uncertainty is statistical and the second is type-B systematic.

p_T^{\min}	p_T^{\max}	$\frac{B_{\phi}}{2\pi p_T} \frac{d^2 N}{dy dp_T} (\text{GeV}/c)^{-2}$				
(GeV/c)		0%–100%	0%–20%	20%–40%	40%–60%	60%–88%
$-2.2 < y < -1.2$						
1.0	2.0	$(4.35 \pm 0.41 \pm 0.65) \times 10^{-7}$	$(1.01 \pm 0.12 \pm 0.15) \times 10^{-6}$	$(6.56 \pm 1.32 \pm 0.98) \times 10^{-7}$	$(4.94 \pm 0.83 \pm 0.74) \times 10^{-7}$	$(1.89 \pm 0.32 \pm 0.28) \times 10^{-7}$
2.0	2.5	$(8.70 \pm 0.75 \pm 1.13) \times 10^{-8}$	$(1.95 \pm 0.19 \pm 0.25) \times 10^{-7}$	$(1.12 \pm 0.17 \pm 0.15) \times 10^{-7}$	$(5.47 \pm 0.87 \pm 0.71) \times 10^{-8}$	$(2.32 \pm 0.44 \pm 0.30) \times 10^{-8}$
2.5	3.0	$(3.09 \pm 0.25 \pm 0.40) \times 10^{-8}$	$(7.35 \pm 0.68 \pm 0.95) \times 10^{-8}$	$(3.68 \pm 0.62 \pm 0.48) \times 10^{-8}$	$(2.23 \pm 0.32 \pm 0.29) \times 10^{-8}$	$(7.05 \pm 1.51 \pm 0.92) \times 10^{-9}$
3.0	4.5	$(2.70 \pm 0.22 \pm 0.35) \times 10^{-9}$	$(5.95 \pm 0.82 \pm 0.77) \times 10^{-9}$	$(3.79 \pm 0.49 \pm 0.49) \times 10^{-9}$	$(1.87 \pm 0.29 \pm 0.24) \times 10^{-9}$	$(6.52 \pm 3.22 \pm 0.85) \times 10^{-10}$
4.5	7.0	$(6.35 \pm 1.72 \pm 0.83) \times 10^{-11}$	$(1.10 \pm 0.39 \pm 0.14) \times 10^{-10}$	$(9.61 \pm 3.51 \pm 1.25) \times 10^{-11}$	$(4.28 \pm 2.40 \pm 0.56) \times 10^{-11}$	$(2.59 \pm 1.04 \pm 0.34) \times 10^{-11}$
$1.2 < y < 2.2$						
1.0	2.0	$(2.00 \pm 0.25 \pm 0.30) \times 10^{-7}$	$(3.37 \pm 0.65 \pm 0.51) \times 10^{-7}$	$(2.93 \pm 0.61 \pm 0.44) \times 10^{-7}$	$(3.47 \pm 0.76 \pm 0.52) \times 10^{-7}$	$(1.82 \pm 0.31 \pm 0.27) \times 10^{-7}$
2.0	2.5	$(3.80 \pm 0.54 \pm 0.49) \times 10^{-8}$	$(9.30 \pm 1.59 \pm 1.21) \times 10^{-8}$	$(5.47 \pm 0.73 \pm 0.71) \times 10^{-8}$	$(4.42 \pm 0.71 \pm 0.57) \times 10^{-8}$	$(2.07 \pm 0.44 \pm 0.27) \times 10^{-8}$
2.5	3.0	$(1.68 \pm 0.18 \pm 0.22) \times 10^{-8}$	$(3.47 \pm 0.56 \pm 0.45) \times 10^{-8}$	$(2.18 \pm 0.37 \pm 0.28) \times 10^{-8}$	$(1.60 \pm 0.25 \pm 0.21) \times 10^{-8}$	$(6.52 \pm 1.07 \pm 0.85) \times 10^{-9}$
3.0	4.5	$(1.48 \pm 0.14 \pm 0.19) \times 10^{-9}$	$(2.60 \pm 0.63 \pm 0.34) \times 10^{-9}$	$(1.80 \pm 0.60 \pm 0.23) \times 10^{-9}$	$(1.44 \pm 0.24 \pm 0.19) \times 10^{-9}$	$(6.24 \pm 1.33 \pm 0.81) \times 10^{-10}$
4.5	7.0	$(6.23 \pm 1.51 \pm 0.81) \times 10^{-11}$	$(1.16 \pm 0.27 \pm 0.15) \times 10^{-10}$	$(7.13 \pm 3.73 \pm 0.93) \times 10^{-11}$	$(5.55 \pm 1.78 \pm 0.72) \times 10^{-11}$	$(2.39 \pm 1.40 \pm 0.31) \times 10^{-11}$
$ y < 0.35$						
0.00	0.25	$(9.81 \pm 2.88 \pm 3.01) \times 10^{-6}$	$(1.93 \pm 0.76 \pm 0.55) \times 10^{-5}$	$(1.23 \pm 0.53 \pm 0.33) \times 10^{-5}$	$(8.92 \pm 4.22 \pm 2.42) \times 10^{-6}$	$(4.87 \pm 2.74 \pm 1.26) \times 10^{-6}$
0.25	0.50	$(7.18 \pm 0.74 \pm 1.57) \times 10^{-6}$	$(1.23 \pm 0.22 \pm 0.23) \times 10^{-5}$	$(1.03 \pm 0.16 \pm 0.22) \times 10^{-5}$	$(5.46 \pm 1.02 \pm 1.05) \times 10^{-6}$	$(4.28 \pm 0.81 \pm 0.81) \times 10^{-6}$
0.50	0.75	$(3.49 \pm 0.35 \pm 0.71) \times 10^{-6}$	$(6.11 \pm 1.00 \pm 1.30) \times 10^{-6}$	$(4.52 \pm 0.69 \pm 0.90) \times 10^{-6}$	$(3.96 \pm 0.54 \pm 0.69) \times 10^{-6}$	$(2.18 \pm 0.36 \pm 0.39) \times 10^{-6}$
0.75	1.00	$(2.19 \pm 0.18 \pm 0.42) \times 10^{-6}$	$(3.54 \pm 0.46 \pm 0.70) \times 10^{-6}$	$(3.13 \pm 0.36 \pm 0.58) \times 10^{-6}$	$(1.54 \pm 0.20 \pm 0.25) \times 10^{-6}$	$(1.28 \pm 0.17 \pm 0.22) \times 10^{-6}$
1.00	1.25	$(1.18 \pm 0.09 \pm 0.21) \times 10^{-6}$	$(2.16 \pm 0.24 \pm 0.40) \times 10^{-6}$	$(1.51 \pm 0.17 \pm 0.27) \times 10^{-6}$	$(7.44 \pm 1.13 \pm 1.21) \times 10^{-7}$	$(5.70 \pm 0.93 \pm 0.93) \times 10^{-7}$
1.25	1.50	$(6.20 \pm 0.49 \pm 1.08) \times 10^{-7}$	$(1.26 \pm 0.14 \pm 0.22) \times 10^{-6}$	$(8.92 \pm 0.99 \pm 1.51) \times 10^{-7}$	$(4.87 \pm 0.67 \pm 0.77) \times 10^{-7}$	$(2.37 \pm 0.38 \pm 0.39) \times 10^{-7}$
1.50	1.75	$(2.75 \pm 0.24 \pm 0.46) \times 10^{-7}$	$(6.32 \pm 0.78 \pm 1.08) \times 10^{-7}$	$(3.13 \pm 0.45 \pm 0.51) \times 10^{-7}$	$(1.90 \pm 0.30 \pm 0.30) \times 10^{-7}$	$(1.65 \pm 0.26 \pm 0.27) \times 10^{-7}$
1.75	2.00	$(1.59 \pm 0.15 \pm 0.26) \times 10^{-7}$	$(3.31 \pm 0.43 \pm 0.55) \times 10^{-7}$	$(2.34 \pm 0.30 \pm 0.37) \times 10^{-7}$	$(1.32 \pm 0.21 \pm 0.21) \times 10^{-7}$	$(4.11 \pm 1.03 \pm 0.67) \times 10^{-8}$
2.00	2.50	$(9.22 \pm 0.62 \pm 1.48) \times 10^{-8}$	$(2.01 \pm 0.18 \pm 0.32) \times 10^{-7}$	$(1.29 \pm 0.12 \pm 0.20) \times 10^{-7}$	$(7.15 \pm 0.85 \pm 1.13) \times 10^{-8}$	$(3.60 \pm 0.56 \pm 0.59) \times 10^{-8}$
2.50	3.00	$(3.19 \pm 0.24 \pm 0.49) \times 10^{-8}$	$(7.12 \pm 0.71 \pm 1.10) \times 10^{-8}$	$(3.54 \pm 0.44 \pm 0.53) \times 10^{-8}$	$(2.84 \pm 0.39 \pm 0.44) \times 10^{-8}$	$(1.10 \pm 0.22 \pm 0.18) \times 10^{-8}$
3.00	4.00	$(6.17 \pm 0.49 \pm 0.94) \times 10^{-9}$	$(1.15 \pm 0.14 \pm 0.18) \times 10^{-8}$	$(8.92 \pm 1.10 \pm 1.36) \times 10^{-9}$	$(5.52 \pm 0.81 \pm 0.88) \times 10^{-9}$	$(1.94 \pm 0.44 \pm 0.33) \times 10^{-9}$
4.00	5.00	$(9.45 \pm 1.25 \pm 1.47) \times 10^{-10}$	$(2.27 \pm 0.37 \pm 0.37) \times 10^{-9}$	$(1.27 \pm 0.26 \pm 0.20) \times 10^{-9}$	$(8.74 \pm 2.06 \pm 1.57) \times 10^{-10}$	$(1.87 \pm 1.10 \pm 0.34) \times 10^{-10}$
5.00	7.00	$(1.02 \pm 0.19 \pm 0.17) \times 10^{-10}$	$(1.46 \pm 0.45 \pm 0.25) \times 10^{-10}$	$(1.98 \pm 0.50 \pm 0.03) \times 10^{-10}$	$(8.27 \pm 3.16 \pm 1.59) \times 10^{-11}$	$(4.79 \pm 2.74 \pm 0.90) \times 10^{-11}$

TABLE IV. R_{dAu} as a function of rapidity of ϕ meson summed over the p_T range, $1 < p_T < 7$ GeV/c for 0%–100% centrality. The first uncertainty is statistical and the second is type-B systematic.

y_{\min}	y_{\max}	R_{dAu}
-2.2	-2.0	$1.23 \pm 0.12 \pm 0.20$
-2.0	-1.7	$1.30 \pm 0.13 \pm 0.21$
-1.7	-1.1	$1.34 \pm 0.13 \pm 0.21$
-0.35	0.35	$1.02 \pm 0.11 \pm 0.07$
1.2	1.7	$0.90 \pm 0.11 \pm 0.13$
1.7	2.0	$0.79 \pm 0.07 \pm 0.11$
2.0	2.2	$0.44 \pm 0.06 \pm 0.06$

TABLE V. R_{dAu} vs N_{coll} of ϕ meson at $1 < p_T < 7$ GeV/c. The first uncertainty is statistical and the second is type-B systematic.

Centrality	$\langle N_{\text{coll}} \rangle$	R_{dAu}		
		$-2.2 < y < -1.2$	$1.2 < y < 2.2$	$ y < 0.35$
0%–20%	15.1 ± 1.0	$1.26 \pm 0.21 \pm 0.21$	$0.73 \pm 0.12 \pm 0.12$	$1.03 \pm 0.11 \pm 0.09$
20%–40%	10.2 ± 0.7	$1.25 \pm 0.20 \pm 0.20$	$0.65 \pm 0.10 \pm 0.11$	$1.00 \pm 0.10 \pm 0.09$
40%–60%	6.6 ± 0.4	$1.18 \pm 0.20 \pm 0.19$	$0.80 \pm 0.11 \pm 0.13$	$0.86 \pm 0.09 \pm 0.08$
60%–88%	3.2 ± 0.2	$1.24 \pm 0.22 \pm 0.20$	$0.95 \pm 0.17 \pm 0.16$	$1.04 \pm 0.11 \pm 0.09$

TABLE VI. R_{dAu} and p_T at different $d+Au$ centrality classes. The first uncertainty is statistical and the second is type-B systematic.

p_T^{\min}	p_T^{\max}	R_{dAu}				
(GeV/c)		0%-100%	0%-20%	20%-40%	40%-60%	60%-88%
				-2.2 < y < -1.2		
1.0	2.0	0.92±0.10±0.12	1.07±0.14±0.14	1.03±0.22±0.13	1.20±0.22±0.16	0.94±0.17±0.12
2.0	2.5	1.57±0.16±0.19	1.78±0.20±0.18	1.51±0.25±0.15	1.14±0.19±0.11	1.00±0.20±0.10
2.5	3.0	2.19±0.22±0.26	2.63±0.29±0.26	1.95±0.35±0.19	1.83±0.28±0.18	1.19±0.26±0.12
3.0	4.5	1.66±0.17±0.20	1.84±0.28±0.18	1.74±0.25±0.17	1.33±0.22±0.13	0.95±0.47±0.10
4.5	7.0	1.03±0.30±0.12	0.90±0.33±0.09	1.17±0.44±0.12	0.80±0.46±0.08	1.00±0.41±0.10
				1.2 < y < 2.2		
1.0	2.0	0.42±0.06±0.05	0.36±0.07±0.05	0.46±0.10±0.06	0.84±0.19±0.11	0.91±0.16±0.12
2.0	2.5	0.69±0.10±0.08	0.85±0.15±0.08	0.74±0.11±0.07	0.92±0.16±0.09	0.89±0.20±0.09
2.5	3.0	1.20±0.14±0.13	1.24±0.21±0.12	1.15±0.21±0.12	1.31±0.22±0.13	1.10±0.19±0.11
3.0	4.5	0.91±0.10±0.10	0.80±0.20±0.08	0.83±0.28±0.08	1.02±0.18±0.10	0.91±0.20±0.09
4.5	7.0	1.01±0.26±0.11	0.95±0.24±0.10	0.87±0.46±0.09	1.04±0.35±0.10	0.92±0.55±0.09
				$ y < 0.35$		
0.00	0.25	0.70±0.29±0.18	0.69±0.33±0.18	0.65±0.33±0.16	0.73±0.40±0.19	0.82±0.51±0.21
0.25	0.50	0.72±0.18±0.08	0.62±0.17±0.07	0.76±0.21±0.08	0.63±0.18±0.07	1.00±0.28±0.11
0.50	0.75	0.74±0.18±0.07	0.65±0.19±0.06	0.71±0.19±0.07	0.97±0.24±0.10	1.10±0.29±0.11
0.75	1.00	0.71±0.15±0.07	0.58±0.14±0.06	0.75±0.16±0.07	0.57±0.12±0.06	0.98±0.21±0.10
1.00	1.25	0.86±0.20±0.09	0.80±0.20±0.08	0.82±0.20±0.08	0.63±0.16±0.06	0.99±0.26±0.10
1.25	1.50	0.89±0.22±0.09	0.91±0.23±0.09	0.95±0.24±0.09	0.81±0.21±0.08	0.81±0.22±0.08
1.50	1.75	0.75±0.18±0.07	0.87±0.22±0.08	0.63±0.16±0.06	0.60±0.16±0.06	1.10±0.28±0.10
1.75	2.00	0.82±0.19±0.08	0.86±0.22±0.08	0.89±0.22±0.09	0.78±0.21±0.08	0.50±0.17±0.05
2.00	2.50	1.20±0.26±0.12	1.30±0.30±0.13	1.20±0.28±0.12	1.10±0.26±0.10	1.10±0.29±0.11
2.50	3.00	1.30±0.29±0.13	1.50±0.34±0.14	1.10±0.26±0.10	1.30±0.33±0.13	1.10±0.31±0.10
3.00	4.00	1.20±0.27±0.13	1.20±0.28±0.12	1.30±0.32±0.13	1.30±0.33±0.13	0.94±0.30±0.09
4.00	5.00	1.30±0.33±0.14	1.60±0.43±0.17	1.30±0.39±0.14	1.40±0.47±0.15	0.63±0.40±0.07
5.00	7.00	1.80±0.54±0.21	1.30±0.52±0.15	2.70±0.91±0.30	1.70±0.80±0.19	2.10±1.30±0.23

-
- 450 [1] K. Adcox *et al.* (PHENIX Collaboration), “Formation of dense partonic matter in relativistic nucleus-nucleus collisions at
451 RHIC: Experimental evaluation by the PHENIX Collaboration,” Nucl. Phys. A **757**, 184 (2005).
- 452 [2] J. Adams *et al.* (STAR Collaboration), “Experimental and theoretical challenges in the search for the quark gluon plasma:
453 The STAR Collaboration’s critical assessment of the evidence from RHIC collisions,” Nucl. Phys. A **757**, 102 (2005).
- 454 [3] J. J. Heckman, J. Seo, and C. Vafa, “Phase Structure of a Brane/Anti-Brane System at Large N ,” J. High Energy Phys.
455 **0707**, 073 (2007).
- 456 [4] I. Vitev, “Initial state parton broadening and energy loss probed in $d+Au$ at RHIC,” Phys. Lett. B **562**, 36 (2003).
- 457 [5] J. W. Cronin, H. J. Frisch, M.J. Shochet, J.P. Boymond, R. Mermod, *et al.*, “Production of Hadrons with Large Transverse
458 Momentum at 200 GeV, 300 GeV, and 400 GeV,” Phys. Rev. D **11**, 3105 (1975).
- 459 [6] A. Accardi and M. Gyulassy, “Cronin effect versus geometrical shadowing in $d+Au$ collisions at RHIC,” Phys. Lett. B
460 **586**, 244 (2004).
- 461 [7] A. Adare *et al.* (PHENIX Collaboration), “Quadrupole Anisotropy in Dihadron Azimuthal Correlations in Central $d+Au$
462 Collisions at $\sqrt{s_{NN}}=200$ GeV,” Phys. Rev. Lett. **111**, 212301 (2013).
- 463 [8] A. Adare *et al.* (PHENIX Collaboration), “Measurement of long-range angular correlation and quadrupole anisotropy of
464 pions and (anti)protons in central $d+Au$ collisions at $\sqrt{s_{NN}}=200$ GeV,” Phys. Rev. Lett. **114**, 192301 (2015).
- 465 [9] B. B. Back *et al.* (PHOBOS Collaboration), “Pseudorapidity distribution of charged particles in $d+Au$ collisions at
466 $\sqrt{s_{NN}}=200$ GeV,” Phys. Rev. Lett. **93**, 082301 (2004).
- 467 [10] B. B. Back *et al.* (PHOBOS Collaboration), “Scaling of charged particle production in $d+Au$ collisions at $\sqrt{s_{NN}}=200$ GeV,”
468 Phys. Rev. C **72**, 031901 (2005).
- 469 [11] I. Arsene *et al.* (BRAHMS Collaboration), “Centrality Dependence of Charged-Particle Pseudorapidity Distributions from
470 $d+Au$ collisions at $\sqrt{s_{NN}}=200$ GeV,” Phys. Rev. Lett. **94**, 032301 (2005).
- 471 [12] B. I. Abelev *et al.* (STAR Collaboration), “Systematic measurements of identified particle spectra in pp, $d+Au$, and
472 $Au+Au$ collisions at the STAR detector,” Phys. Rev. C **79**, 034909 (2009).
- 473 [13] S. Chatrchyan *et al.* (CMS Collaboration), “Observation of long-range near-side angular correlations in proton-lead colli-
474 sions at the LHC,” Phys. Lett. B **718**, 795 (2013).
- 475 [14] G. Aad *et al.* (ATLAS Collaboration), “Observation of Associated Near-Side and Away-Side Long-Range Correlations in
476 $\sqrt{s_{NN}}=5.02$ TeV Proton-Lead Collisions with the ATLAS Detector,” Phys. Rev. Lett. **110**, 182302 (2013).
- 477 [15] S. Chatrchyan *et al.* (CMS Collaboration), “Multiplicity and transverse momentum dependence of two- and four-particle
478 correlations in pPb and $PbPb$ collisions,” Phys. Lett. B **724**, 213 (2013).
- 479 [16] G. Aad *et al.* (ATLAS Collaboration), “Measurement with the ATLAS detector of multi-particle azimuthal correlations in
480 $p+Pb$ collisions at $\sqrt{s_{NN}}=5.02$ TeV,” Phys. Lett. B **725**, 60 (2013).
- 481 [17] B. B. Abelev *et al.* (ALICE Collaboration), “Long-range angular correlations of π , K , and p in p -Pb collisions at $\sqrt{s_{NN}}$
482 $= 5.02$ TeV,” Phys. Lett. B **726**, 164 (2013).
- 483 [18] G. Aad *et al.* (ATLAS Collaboration), “Measurement of long-range pseudorapidity correlations and azimuthal harmonics
484 in $\sqrt{s_{NN}} = 5.02$ TeV proton-lead collisions with the ATLAS detector,” Phys. Rev. C **90**, 044906 (2014).
- 485 [19] B. B. Abelev *et al.* (ALICE Collaboration), “Multiparticle azimuthal correlations in p -Pb and Pb-Pb collisions at the
486 CERN Large Hadron Collider,” Phys. Rev. C **90**, 054901 (2014).
- 487 [20] L. Adamczyk *et al.* (STAR Collaboration), “Long-range pseudorapidity dihadron correlations in $d+Au$ collisions at
488 $\sqrt{s_{NN}}=5.02$ GeV,” Phys. Lett. B **747**, 265 (2015).
- 489 [21] A. Adare *et al.* (PHENIX Collaboration), “Transverse-Momentum Dependence of the J/ψ Nuclear Modification in $d+Au$
490 Collisions at $\sqrt{s_{NN}}=200$ GeV,” Phys. Rev. C **87**, 034904 (2013).
- 491 [22] A. Adare *et al.* (PHENIX Collaboration), “Cold-nuclear-matter effects on heavy-quark production in $d+Au$ collisions at
492 $\sqrt{s_{NN}}=200$ GeV,” Phys. Rev. Lett. **109**, 242301 (2012).
- 493 [23] A. Adare *et al.* (PHENIX Collaboration), “ $\Upsilon(1S + 2S + 3S)$ production in $d+Au$ and $p+p$ collisions at $\sqrt{s_{NN}}=200$ GeV
494 and cold-nuclear matter effects,” Phys. Rev. C **87**, 044909 (2013).
- 495 [24] A. Adare *et al.* (PHENIX Collaboration), “Spectra and ratios of identified particles in $Au+Au$ and $d+Au$ collisions at
496 $\sqrt{s_{NN}}=200$ GeV,” Phys. Rev. C **88**, 024906 (2013).
- 497 [25] A. Adare *et al.* (PHENIX Collaboration), “Nuclear Modification of ψ' , χ_c , and J/ψ Production in $d+Au$ Collisions at
498 $\sqrt{s_{NN}}=200$ GeV,” Phys. Rev. Lett. **111**, 202301 (2013).
- 499 [26] A. Adare *et al.* (PHENIX Collaboration), “Cold-Nuclear-Matter Effects on Heavy-Quark Production at Forward and
500 Backward Rapidity in $d+Au$ Collisions at $\sqrt{s_{NN}}=200$ GeV,” Phys. Rev. Lett. **112**, 252301 (2014).
- 501 [27] P. Koch, B. Muller, and J. Rafelski, “Strangeness in Relativistic Heavy Ion Collisions,” Phys.Rept. **142**, 167 (1986).
- 502 [28] A. Shor, “Phi meson production as a probe of the quark gluon plasma,” Phys. Rev. Lett. **54**, 1122 (1985).
- 503 [29] B. Alessandro *et al.* (NA50 Collaboration), “Phi production in Pb-Pb collisions at 158 GeV/ c per nucleon incident mo-
504 mentum,” Phys. Lett. B **555**, 147 (2003).
- 505 [30] S. S. Adler *et al.* (PHENIX Collaboration), “Production of phi mesons at mid-rapidity in $\sqrt{s_{NN}}=200$ GeV $Au+Au$ collisions
506 at RHIC,” Phys. Rev. C **72**, 014903 (2005).
- 507 [31] S. Afanasiev *et al.* (PHENIX Collaboration), “Elliptic flow for phi mesons and (anti)deuterons in $Au + Au$ collisions at
508 $\sqrt{s_{NN}}=200$ GeV,” Phys. Rev. Lett. **99**, 052301 (2007).
- 509 [32] B. I. Abelev *et al.* (STAR Collaboration), “Partonic flow and phi-meson production in $Au+Au$ collisions at $\sqrt{s_{NN}} =$
510 200 GeV,” Phys. Rev. Lett. **99**, 112301 (2007).

- 511 [33] D. Adamova *et al.* (CERES Collaboration), “Modification of the rho-meson detected by low-mass electron-positron pairs
512 in central Pb-Au collisions at 158-A GeV/c,” *Phys. Lett. B* **666**, 425 (2008).
- 513 [34] C. Alt *et al.* (NA49 Collaboration), “Energy dependence of phi meson production in central Pb+Pb collisions at $\sqrt{s_{NN}}=6$
514 to 17 GeV,” *Phys. Rev. C* **78**, 044907 (2008).
- 515 [35] B. I. Abelev *et al.* (STAR Collaboration), “Energy and system size dependence of phi meson production in Cu+Cu and
516 Au+Au collisions,” *Phys. Lett. B* **673**, 183 (2009).
- 517 [36] A. Adare *et al.* (PHENIX Collaboration), “Nuclear modification factors of ϕ mesons in d +Au, Cu+Cu and Au+Au
518 collisions at $\sqrt{s_{NN}}=200$ GeV,” *Phys. Rev. C* **83**, 024909 (2011).
- 519 [37] R. Arnaldi *et al.* (NA60 Collaboration), “A Comparative measurement of $\phi \rightarrow K^+K^-$ and $\phi \rightarrow \mu^+\mu^-$ in In-In collisions
520 at the CERN SPS,” *Phys. Lett. B* **699**, 325 (2011).
- 521 [38] A. Adare *et al.* (PHENIX Collaboration), “Measurement of neutral mesons in $p+p$ collisions at $\sqrt{s}=200$ GeV and scaling
522 properties of hadron production,” *Phys. Rev. D* **83**, 052004 (2011).
- 523 [39] A. Adare *et al.* (PHENIX Collaboration), “Low-mass vector-meson production at forward rapidity in $p+p$ collisions at
524 $\sqrt{s}=200$ GeV,” *Phys. Rev. D* **90**, 052002 (2014).
- 525 [40] K. Adcox *et al.* (PHENIX Collaboration), “PHENIX detector overview,” *Nucl. Instrum. Methods Phys. Res., Sec. A* **499**,
526 469 (2003).
- 527 [41] J. Beringer *et al.* (Particle Data Group), “Rev. of Particle Phys. (RPP),” *Phys. Rev. D* **86**, 010001 (2012).
- 528 [42] W. M. Yao *et al.* (Particle Data Group), “Review of Particle Physics,” *J. Phys. G* **33**, 1 (2006).
- 529 [43] T. Sjostrand, P. Eden, C. Friberg, L. Lonnblad, G. Miu, S. Mrenna, and E. Norrbin, “High-energy physics event generation
530 with PYTHIA 6.1,” *Comput. Phys. Commun.* **135**, 238 (2001).
- 531 [44] *GEANT 3.2.1 Manual* (1994), CERN W5013.
- 532 [45] A. Adare *et al.* (PHENIX Collaboration), “Production of ω mesons in $p+p$, d +Au, Cu+Cu, and Au+Au collisions at
533 $\sqrt{s_{NN}}=200$ GeV,” *Phys. Rev. C* **84**, 044902 (2011).
- 534 [46] A. Adare *et al.* (PHENIX Collaboration), “Detailed measurement of the e^+e^- pair continuum in $p+p$ and Au+Au collisions
535 at $\sqrt{s_{NN}}=200$ GeV and implications for direct photon production,” *Phys. Rev. C* **81**, 034911 (2010).
- 536 [47] A. Adare *et al.* (PHENIX Collaboration), “Centrality categorization for $R_{p(d)+A}$ in high-energy collisions,” *Phys. Rev. C*
537 **90**, 034902 (2014).
- 538 [48] S. S. Adler *et al.* (PHENIX Collaboration), “ J/ψ production and nuclear effects for d +Au and $p+p$ collisions at
539 $\sqrt{s_{NN}}=200$ GeV,” *Phys. Rev. Lett.* **96**, 012304 (2006).
- 540 [49] G. D. Lafferty and T.R. Wyatt, “Where to stick your data points: The treatment of measurements within wide bins,”
541 *Nucl. Instrum. Methods Phys. Res., Sec. A* **355**, 541 (1995).
- 542 [50] R. Hagedorn, “Statistical thermodynamics of strong interactions at high-energies,” *Nuovo Cim. Suppl.* **3**, 147 (1965).
- 543 [51] D. M. Kaplan *et al.* (FNAL-E288 Collaboration), “Study of the High Mass Dimuon Continuum in 400 GeV Proton-Nucleus
544 Collisions,” *Phys. Rev. Lett.* **40**, 435 (1978).
- 545 [52] A. Adare *et al.* (PHENIX Collaboration), “Cold Nuclear Matter Effects on J/ψ Yields as a Function of Rapidity and
546 Nuclear Geometry in Deuteron-Gold Collisions at $\sqrt{s_{NN}}=200$ GeV,” *Phys. Rev. Lett.* **107**, 142301 (2011).
- 547 [53] J. Adam *et al.* (ALICE Collaboration), “phi-meson production at forward rapidity in $p+Pb$ collisions at $\sqrt{s_{NN}}=5.02$ TeV
548 and in $p+p$ collisions at $\sqrt{s}=2.86$ TeV,” arXiv:1506.09206.